IEEE Access
Multidisciplinary | Rapid Review | Open Access Journal

Digital Object Identifier xx.xxxx/ACCESS.20xx.DOI

UAV-IoUT: Empirical Characterization and Energy Efficient Data Collection in UAV-enabled Internet of Underground Things

SYED MUHAMMAD HASHIR[1,4], MEHMET C. VURAN[2], (Member, IEEE), DINESH RAJAN[1], (Senior Member, IEEE), MANINDERPAL SINGH[1,3], (Member, IEEE), JOSEPH CAMP[1], (Senior Member, IEEE)

[1]Department of Electrical and Computer Engineering, Southern Methodist University, Dallas, TX, USA (e-mail: {rajand, maninderpals, camp}@smu.edu)
[2]School of Computing, University of Nebraska-Lincoln, Lincoln, NE, USA (e-mail: mcv@unl.edu)
[3]Department of Engineering Technology, University of Houston, Houston, TX, USA (e-mail: msingh28@uh.edu)
[4]Department of Engineering Technology, University of Kentucky, Paducah, KY, USA (e-mail: mhashirs@uky.edu)

Corresponding author: Syed Muhammad Hashir (e-mail: mhashirs@uky.edu).

ABSTRACT Unmanned Aerial Vehicles (UAVs) have emerged as highly adaptable equipment in modern agriculture, transforming traditional farming practices with data-driven decision-making to improve crop yields. While UAVs are mainly employed for aerial imaging and surveillance, their potential for collecting underground (UG) sensor data is underexplored. This paper investigates the path loss and fading characteristics between UAV and UG nodes using outdoor measurements, to facilitate energy-efficient data collection for air-to-underground wireless links. We show significant impacts from UAV antenna position, UAV 3D location, and soil properties on both path loss and fading. A novel channel model is developed that estimates the path loss with an average RMSE improvement of 3.16 dB and a maximum improvement of up to 10.45 dB over previous models in various 3D positions of the UAV. The analysis extends to the fading distribution within the channel, which conforms to the Rician distribution, where the Rician-K is contingent upon the UAV's altitude, elevation angle, and antenna configurations. Specifically, two Gaussian functions are derived to capture the effects attributed to the altitude and elevation angle, with root mean square errors (RMSEs) of 2.86 dB – 4.38 dB and 2.1 dB – 6.1 dB, respectively. The developed model is employed to drive an energy-efficient data collection strategy, *UAV-Collect*, for UAV-aided Internet of Underground Things. UAV-Collect substantially reduces the energy use of UG sensor nodes. Our approach has the potential to optimize resources on UAV and UG nodes, enabling efficient agricultural monitoring.

INDEX TERMS UAV, underground communication, precision agriculture, IoT, energy minimization.

I. INTRODUCTION

The Internet of Underground Things (IoUT) is a growing field that has applications in a variety of commercial and non-commercial sectors like agriculture and petroleum [1], [2]. Often underground (UG) sensors are deployed for different purposes in these application areas (*e.g.*, environment monitoring, geophysical studies, and assessment of infrastructural health). Some commonly used UG sensors include seismic sensors, moisture sensors, temperature sensors, and chemical sensors [3]. All of these sensors behave differently in terms of their characteristics, and there are possible signal characterization differences for different soil types, moisture content, sensor depth, and other factors [4], [5].The primary goal behind the deployment of these sensors is to collect data from subsurface environments and accurately characterize their underlying properties. Hence, empirical analysis is crucial across several key areas: signal behavior, system design and optimization, performance evaluation, deployment strategies, adaptability to changing conditions, interference and noise mitigation, and model validation. In particular, empirical signal characterization in UG sensors becomes essential to design, optimize, and deploy sensor systems that can operate

reliably in dynamic and complex UG environments [6]–[8].

There are several methods for collecting data from UG sensors, each with its own set of advantages and limitations. One common approach involves creating clusters of UG sensors and employing fixed aboveground (AG) communication points to relay the collected data to a central destination [3]. Although this method can be effective, it is heavily based on a fixed AG infrastructure, which can be costly and challenging to deploy in certain environments. In addition, the approach is constrained by the communication range and the energy required to transmit data to and from sensors.

To overcome these challenges, there have been substantial advancements in standalone UG devices, integrating both sensor and communication technologies [9], [10]. This progress has been pivotal in the advancement of the IoUT. These innovative devices are designed to operate effectively in complex and often harsh environments, such as soil, tunnels, and underground mines, where environmental conditions can severely impact their connectivity with AG systems. Moreover, scaling IoUT presents additional challenges due to the limited connectivity infrastructure in rural areas, leading to smaller and more expensive networks. Increasing the transmission power of UG devices could potentially extend their communication range, but results in higher power consumption, which in turn shortens the operation lifetime of these battery-operated devices.

Unmanned Aerial Vehicles (UAVs) present a promising alternative to traditional data collection methods in IoUT. UAVs can gather data from UG sensors more efficiently, potentially reducing both power consumption and data collection time [11]. Their maneuverability and flexibility enable them to support network scalability with reduced deployment costs, thereby minimizing the need for numerous fixed AG nodes. UAV-enabled sensing has also been explored using multimodal feature integration for detection and signal characterization tasks. In [12], audio and visual features are jointly leveraged to enhance the reliability of UAV detection in public safety applications. Despite these advantages, the radio propagation characteristics of Air-to-Underground (Air2UG) and Underground-to-Air (UG2Air) channels are not yet well understood and require further investigation to fully leverage UAVs in this context.

In this work, we analyze and model the large and small-scale wireless channel characteristics of the Air2UG and UG2Air links using in-field measurements between a UAV and UG nodes under dynamic UAV 3D locations, UAV antenna positions, and UG soil conditions. Accordingly, a UAV-aided IoUT system is explored to develop an energy-efficient data collection mechanism that has the potential to serve as an application for novel empirical findings of the proposed work. The contributions of the proposed work are:

- Measurements of the reflection coefficient or S_{11} of a wide-band antenna with and without the drone body are performed, which suggests that the impacts of the drone body are significant on the antenna characteristics, with a maximum change in S_{11} of 15 dB, surpassing the -10 dB threshold.
- We show that the antenna position on the drone has a noticeable impact on the path loss and fading in the channel. Findings suggest the antenna mounted on the bottom plate of the UAV provides lower path loss and higher Rician-K performance than the antenna mounted on the UAV's arm.
- Channel characteristics in the Air2UG and UG2Air channels are observed, and it is found that the two are nearly equal and may be modeled identically. Based on this, a new path loss model is proposed that estimates the path loss in both directions of the considered channel at various UAV 3D positions with RMSE between 1.88 dB – 8.52 dB and errors less than the AG2UG model in [7].
- Findings suggest that the fading in the Air2UG and UG2Air channels follows a Rician distribution, and Rician-K is dependent on the altitude and elevation angle of the UAV. Using two Gaussian functions, we capture the altitude and elevation angle, with RMSEs of 2.86 dB – 4.38 dB for altitude and 1.89 dB – 6.1 dB for elevation angle.
- Finally, we cast a UAV-aided energy minimization data collection problem with UG sensors based on empirical channel models. The formulated problem reduces the peak energy consumption across the UG sensors by jointly optimizing the 3D trajectory of the UAV, transmission scheduling, and uplink transmit power, while ensuring that the data demands of all sensors are met. The problem is non-convex, which makes finding an optimal solution challenging. To address this, we decompose the original problem into smaller, more tractable subproblems, which are then solved independently. Accordingly, an energy-efficient data collection scheme, *UAV-Collect*, capable of achieving up to $12\times$ lower energy consumption on the UG sensors compared to the benchmark schemes, is developed.

The remainder of the paper is organized as follows: In Section II, related work on UG communications and UAV-aided data collection is discussed. In Section III, the path loss and fading models for UG communications are described. Section IV outlines the experimental setup, measurement procedures, and soil parameters associated with the measurement location. Section V presents the empirical results obtained in dynamic measurement scenarios along with their comparisons. In Section VI, a UAV-aided IoUT is presented as an application for our empirical findings, and an energy-energy efficient data collection scheme is proposed. Finally, the paper is concluded in Section VII.

II. RELATED WORK

In a soil medium, the properties of the soil and their dynamics on the channel mostly affect the connection quality [13]. Furthermore, the soil-air interface also plays a significant role in the two-way communication that causes reflection, refraction, and attenuation in the electromagnetic signals.

The radio signal propagation characteristics between AG and UG communication nodes have been extensively studied in the literature for both AG2UG and UG2AG links [7], [13], [14]. In [13], empirical characterization in AG2UG and UG2AG links was considered, where the measurements were conducted in an agricultural field. The findings demonstrate a significant variation between below-ground and aboveground communications, with the former being strongly dependent on burial depth and soil moisture. Similarly, in [15], UG communication links were evaluated to model statistical propagation characteristics, where the impact of soil type, soil moisture, antenna depth, and transmission frequency on the channel was demonstrated.

The communication links between UAV and UG nodes were considered in limited works. In [16], a UAV is utilized to collect sensor data from UG LoRa nodes at various depths, to characterize the impact of increasing sensor depth and the UAV's altitude on the signal strength of LoRa communications. In [17], the feasibility of using UAVs for data collection in IoUT is demonstrated, addressing the issue of high signal attenuation in soil. Experimental results show that UAVs can effectively collect data in both hovering and dynamic modes, with optimized trajectories. In an earlier version of this work [11], we model path loss and fading characteristics in the Air2UG channels (downlink) through real outdoor measurement between a UAV and various UG nodes, where it is shown that the fading in the channel follows a Rician distribution with a strong dependency of altitude on the Rician-K factor. Related methods, such as the polynomial approximation framework in [18], illustrate how UAV sensing and data processing can remain robust under variations in viewpoint or environmental conditions, highlighting challenges similar to those encountered in UG communication measurements. In this work, we extend our previous research in [11] to conduct a more comprehensive analysis. We investigate the impact of UAV body and 3D positioning on bidirectional communication between UAVs and UG sensor nodes through empirical field measurements. Leveraging the empirical findings, we develop efficient path loss and small-scale fading models for the Air2UG/UG2Air link. Building on these models, we propose an energy-efficient aerial data collection framework in IoUT, optimizing the UAV trajectory, resource utilization, and minimizing power consumption in UG sensors.

UAVs have been utilized in many prior works for efficient data collection from over-the-ground sensing nodes in IoT, where the researchers mostly focused on either minimizing the UAV's flight time and the energy consumption of the ground sensors or maximizing the communication rate while completing the data collection task [19]–[21]. In [19], a UAV-enabled wireless sensor network is considered with practical air-to-ground (A2G) Rician fading channels between a UAV and multiple AG sensor nodes, where the objective is to optimize the minimal average data collection rate from all nodes while adhering to reliability constraints. In [20], a similar network is considered to design a data collection strategy with a focus on minimizing the energy consumption of the nodes. In [21], the authors consider multiple UAVs in a wireless sensor network for data collection, where the UAV trajectory, wake-up scheduling, and association for nodes are optimized to reduce the maximum mission completion time while making certain that every node can reliably upload the desired amount of data within the allotted energy limit.

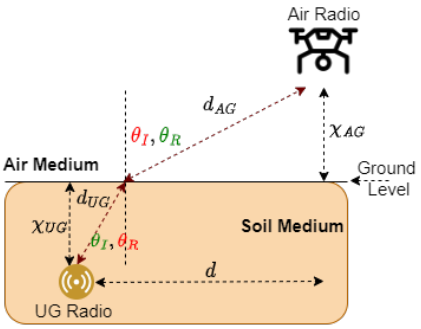

FIGURE 1: Downlink/uplink channels between radios in the air and underground.

Recent studies also highlight the effectiveness of UAVs in collecting data from ground sensors in large fields. In [22], researchers propose a new method that utilizes the LoRa protocol and a Packet Reception Ratio model to enhance data collection through UAVs while reducing energy consumption. An Energy Consumption and Data Acquisition Efficiency optimization problem is formulated, and a solution is presented using Deep Reinforcement Learning that reduces total energy costs compared to prior methods. In [23], authors investigate the potential of data from wireless sensors deployed in large agricultural areas to enhance precision farming tasks, such as irrigation management and fertilization. The authors propose joint clustering and multi-UAV-assisted data-gathering methods to reduce energy consumption and extend sensor battery life. Despite these advancements, the literature on efficient data collection methods in IoUT, particularly with UAVs, remains scarce.

III. AIR2UG CHANNEL MODEL

In this section, we develop new models for large-scale and small-scale radio propagation (*i.e.*, path loss and fading) for the Air2UG channel. The communication channel between aerial and UG nodes are presented in Fig. 1, where the channel in the downward direction corresponds to the downlink (Air2UG) channel while the upward direction channel refers to the uplink (UG2Air) channel, χ_{UG} is the depth of the UG node in the soil, χ_{AG} is the height of the air node, d_{AG} and d_{UG} are the length of the AG and UG components of the channel, and θ_I and θ_R are the incident and refractive angles with green text color showing the angles in the uplink channel and red text color showing the angles in the downlink channel, respectively.

In the following, both large- and small-scale models for the Air2UG channel are provided. We first provide background on existing models in this area, and then present the Air2UG

channel model components.

A. PATH LOSS MODEL

1) Background

The path loss models of the links between a UG node and a stationary AG node are well studied in [7], [13], [14], [24]. The communication link between the nodes in Fig. 1 consists of UG and AG radio propagation paths, where the former path corresponds to propagation in the soil medium and the latter refers to propagation in the air medium. The radio propagation path loss is defined as:

$$PL^{\rightarrow}[dB] = PL_{UG}(d_{UG}) + PL_{OTA}(d_{AG}) + PL_R^{\rightarrow}, \quad (1)$$

where the superscript $\rightarrow$ shows the propagation direction, i.e., uplink or downlink, PL_{UG} is the path loss associated with the UG path that depends on the signal path distance between the UG node and the ground surface d_{UG}. Similarly, PL_{OTA} is the path loss in the air medium that depends on the over-the-air (OTA) signal path distance d_{AG}. $PL_R^{\rightarrow}$ is the refraction loss caused by the air-soil interface, which is dependent on the propagation direction in the uplink and downlink. The individual path loss terms in (1) are defined as follows [7]:

$$PL_{UG}(d_{UG}) = 6.4 + 20\log(d_{UG}) + 20\log(\beta) + 8.69\alpha d_{UG}, \quad (2)$$

$$PL_{OTA}(d_{AG}) = -147.6 + 10\eta\log(d_{AG}) + 20\log(f), \quad (3)$$

$$PL_R^{DL} = 10\log\frac{\left(\cos\theta_I + \sqrt{\epsilon_s^{'} - \sin^2(\theta_I)}\right)^2}{4\cos\theta_I\sqrt{\epsilon_s^{'} - \sin^2(\theta_I)}}, \quad (4)$$

$$PL_R^{UL} = 10\log\frac{\left(1 + \sqrt{\epsilon_s^{'}}\right)^2}{4\sqrt{\epsilon_s^{'}}}, \quad (5)$$

where α and β refer to the attenuation and phase shift of the wave in soil, respectively, η corresponds to the AG attenuation coefficient, f is the carrier frequency of the propagating signal, $\epsilon_s^{'}$ is the real part of the relative dielectric constant of the soil-water mixture, θ_I is the angle of incidence, PL_R^{DL} is the refraction loss in the downlink direction, and PL_R^{UL} is the refraction loss in the uplink direction. Note that PL_R^{UL} is independent of θ_I and θ_R in [7], based on the assumption that $\chi_{AG} \ll d_{AG}$, which leads to $d \approx d_{AG}$. However, this assumption is not valid for UAVs and will be discussed later in this section.

The permittivity of the soil, which depends on soil properties such as moisture, texture, and bulk density, has a major influence on signal propagation in the soil medium. Therefore, the impact of soil permittivity on wireless propagation has been characterized. The complex-valued permittivity of the soil can be defined as $\epsilon_s = \epsilon_s^{'} - \iota\epsilon_s^{''}$, where $\epsilon_s^{'}$ and $\epsilon_s^{''}$ are the real and imaginary parts of the relative permittivity of the soil. In [25], $\epsilon_s^{'}$ and $\epsilon_s^{''}$ are experimentally characterized for the frequency range of 300 MHz – 1300 MHz as $\epsilon_s^{'} = (1.15[1 + \frac{\rho_b}{\rho_s}(\epsilon_m^{\delta} - 1) + (m_v)^{v^{'}}(\epsilon_{fw}^{'})^{\delta} - m_v]^{\frac{1}{\delta}} - 0.68)$ and $\epsilon_s^{''} = [(m_v)^{v^{''}}(\epsilon_{fw}^{''})^{\delta}]^{\frac{1}{\delta}}$, where ρ_b and ρ_s represent the bulk density and particle density of the soil, respectively. m_v is the volumetric moisture content, ϵ_m is the dielectric constant of the soil solids which is defined as $\epsilon_m = (1.01 + 0.44\rho_s)^2 - 0.062$, $\delta = 0.65$ is the constant that is determined empirically, $v^{'}$ and $v^{''}$ are the constants that are dependent on the soil and defined as $v^{'} = 1.2748 - 0.519S - 0.152C$ and $v^{''} = 1.33797 - 0.603S - 0.166C$, where C and S are the mass fractions of clay and sand in the soil mixture, respectively. $\epsilon_{fw}^{'}$, and $\epsilon_{fw}^{''}$ are the real and imaginary parts of the dielectric constant of water, which are described in [5], [24], [25]. Furthermore, the complex propagation constant γ of the electromagnetic wave in the soil is defined as $\gamma = \beta + \iota\alpha$, where α and β can be determined as follows [7]:

$$\alpha = \omega\sqrt{\frac{\mu\epsilon_s^{'}}{2}\left[\sqrt{1 + \left(\frac{\epsilon_s^{''}}{\epsilon_s^{'}}\right)^2} - 1\right]}, \quad (6)$$

$$\beta = \omega\sqrt{\frac{\mu\epsilon_s^{'}}{2}\left[\sqrt{1 + \left(\frac{\epsilon_s^{''}}{\epsilon_s^{'}}\right)^2} + 1\right]}, \quad (7)$$

where ω is the angular velocity and μ is the magnetic permeability of the soil.

Given a transmit power, P_{TX}, the received power, P_{RX}, can be written in logarithmic form as [26]:

$$P_{RX}^{\rightarrow} = P_{TX} + G_{UG} + G_{AG} + 10\log_{10}\left(1 - 10^{-\frac{RL_{UG}}{10}}\right) - PL^{\rightarrow}, \quad (8)$$

where G_{UG} and G_{AG} are the UG and AG antenna gains, respectively, and RL_{UG} corresponds to the return loss of the antenna in the soil medium. It is widely known that the antenna's return loss changes when buried in the soil [8]. The variation in return loss is because of the impedance mismatch of the antenna, which is determined by the changes in the permittivity of the soil and reflection from the soil-air interface at a given depth. Therefore, the resonant frequency of an antenna changes due to the variations in signal wavelength because of the soil properties.

2) Air2UG Path Loss Model

The downlink channel between a UAV and a UG node, when the UAV is vertically aligned with the UG node, follows the path loss model given in (1) [11]. However, the uplink communication scenario is different with UAVs compared to the fixed AG node. In the case of uplink communication between a stationary AG node and a UG node, the refraction loss is typically modeled without accounting for the incident or refractive angle. This simplification is based on the assumption that the height of the AG node is significantly smaller than the horizontal distance between the AG and UG nodes, making the slant range approximately equal to the horizontal distance. However, such assumptions are not applicable to the UG2Air link, for two key reasons. First,

the operating altitude of a UAV is generally much higher than that of fixed AG nodes due to infrastructure clearance and safety regulations. Second, UAVs can easily fly directly above or in close proximity to UG nodes for data collection. As a result, the incident angle becomes a critical factor in modeling refraction loss for UAV uplink scenarios, and the simplified approach used in (5) is no longer valid.

Moreover, while the path loss model in (1) provides a useful foundation, it does not capture elevation angle-dependent losses in the AG portion of the communication path between a UAV and a UG node. Previous studies have shown that path loss between a UAV and an AG node is influenced not only by direct distance but also significantly by elevation angle, even when there is a clear line of sight (LoS) between the transmitter and receiver [27], [28]. The elevation angle introduces additional losses due to two main factors: variation in antenna radiation pattern gain at different angles, especially the reduced gain when the elevation angle falls outside the antenna's main lobe, and increased signal interaction with the ground and surrounding environment, leading to multipath fading and scattering effects. As the elevation angle decreases, the signal path becomes less affected by such interactions, generally resulting in reduced path loss. These effects make the elevation angle an important consideration in modeling UAV-based communication links, regardless of LoS availability. Building on this, we propose an enhanced path loss model that incorporates UAV altitude and elevation angle, offering improved accuracy for both Air2UG and UG2Air communication scenarios, as follows:

$$PL[dB] = PL_{UG}(d_{UG}) + PL_{OTA}(d_{AG}) + PL_R + \Psi(\theta)\ , \tag{9}$$

where $PL_{UG}(d_{UG})$ is defined in (2), $PL_{OTA}(d_{AG})$ is defined in (3), and $\Psi(\theta)$ denotes the elevation angle dependent excess loss in the OTA path of the A2UG channel. The OTA path depends on the elevation angle due to LoS geometry, ground-reflected components, and elevation dependent antenna radiation characteristics. The elevation angle correction term is given by

$$\Psi(\theta) = k_1\left[1 - \cos(k_2\theta) - k_3\sin(k_4\theta)\right]\ , \tag{10}$$

where k_1, k_2, k_3, and k_4 are empirically determined parameters, and θ is the elevation angle between the UAV and UG node. The in-field measurements show additional angular dependence of path loss, including both monotonic and non-monotonic trends with asymmetric slopes influenced by antenna placement. To capture these observed trends, the term $1-\cos(k_2\theta)$ in (10) models the dominant monotonic increase in path loss with elevation angle, consistent with geometric propagation effects and gradual reduction in antenna gain at higher angles. The sine term, $k_3\sin(k_4\theta)$, introduces controlled asymmetry to reproduce non-monotonic trends observed in measurements, such as an initial decrease followed by an increase in path loss at certain elevation angles. The parameters regulate the magnitude and angular sensitivity of the correction, with k_3 controlling the contribution of the asymmetric component. When path loss exhibits predominantly monotonic behavior, a small k_3 reduces the sine contribution, preserving near-monotonic growth. Accordingly, $\Psi(\theta)$ provides a smooth, bounded, and physically consistent representation of residual elevation angle effects. Finally, the refraction loss term PL_R is based on the Fresnel transmission coefficient at the air–soil interface, which preserves the full angular dependence of the transmitted wave. In the prior AG2UG model, this approach was applied only to the downlink, while the uplink neglected the angular dependence under the small height approximation. In the proposed model, we adopt the downlink refraction loss expression from (4) for both uplink and downlink, providing a consistent and physically valid representation of refraction effects over a wide range of elevation angles observed in practical UAV deployments for UG communications.

$$PL_R = 10\log\frac{\left(\cos\theta + \sqrt{\epsilon_s' - \sin^2(\theta)}\right)^2}{4\cos\theta\sqrt{\epsilon_s' - \sin^2(\theta)}}. \tag{11}$$

For practical UAV and UG sensor deployments, where $\chi_{\text{AG}} \gg \chi_{\text{UG}}$ and $\chi_{\text{AG}} \gg d$, θ closely approximates θ_I and θ_R in the Air2UG and UG2Air channels in Fig. 1, as the resulting elevation angles are shallow and the difference between the elevation and actual incident or refracted angles is minimal. The path loss model in (9) is an extension of the model in (1). At a 0-degree elevation angle, $\Psi(\theta) = 0$ and (9) reduces to (1).

B. SMALL-SCALE FADING MODEL

1) Background

The small-scale fading in the AG situation has been extensively studied in the literature for communication between the aerial node and the ground node [19], [29], [30]. In [30], the small-scale fading in the A2G channel is empirically characterized with a Rician distribution, and the Rician-K factor in the channel is found to be significantly dependent on the elevation angle between the communicating nodes. Accordingly, the Rician-K factor (K) as a function of the elevation angle in the A2G channel is modeled as follows [19]:

$$K(\theta) = A_1 \times e^{A_2\times(\frac{\pi}{2}-\theta)}, \tag{12}$$

where $\theta = \arcsin(\chi_{AG}/d_{AG})$ is the elevation angle between the aerial and ground nodes, and A_1 and A_2 are the environmental dependent constant coefficients which are determined as $K_{\min} = A_1$ and $K_{\max} = A_1 \times e^{A_2\times\frac{\pi}{2}}$ with $K_{\min}$ and $K_{\max}$ being the minimum and maximum Rician-K factor in the environment.

The small-scale fading in the UG communication is discussed in the prior work mainly for the communication between the nodes in the soil medium, where both the transmitter and receiver nodes are buried at certain depths [5], [24]. In [5], the communication between two UG nodes

is considered, where the signal propagation between the nodes that are buried near the ground surface comprises the direct path and the ground surface reflected path. The reflected path can be neglected when the UG nodes are buried at high depths. Moreover, the UG channel is considered a multipath Rayleigh fading channel where the randomness in the channel is due to the location of the nodes in the soil as opposed to the time. Thus, each path in the channel is Rayleigh-distributed, and the signal envelope from each path is modeled as an independent Rayleigh-distributed random variable.

In our previous work, we found that small-scale fading in the Air2UG channel with UG nodes buried at depths of 0.1 m and 0.2 m follows a Rician distribution with a strong Rician-K factor that depends on the altitude of the UAV [11]. This observation means that signal propagation in the Air2UG channel has a stronger direct path component compared to the reflected or scattered path components. The propagation of the signal from the air to the soil medium does not reduce the power of the direct path component. As a result, the power of the direct component remains much higher than that of the reflected or scattered components.

2) Air2UG Small-Scale Fading Model

Our empirical analysis shows that fading follows a Rician distribution, with parameters that vary as a function of UAV altitude and elevation angle in both uplink and downlink channels. While simplified UAV channel models often assume monotonic Rician-K trends [19], our measurements indicate that Rician-K behavior depends strongly on antenna placement and the surrounding environment. Specifically, for a multirotor UAV, the bottom-mounted antenna exhibits an initial increase in Rician-K with altitude followed by a decrease due to the interplay of direct LoS paths and multipath from the ground, nearby trees, and structures, whereas the arm-mounted antenna shows a monotonically decreasing Rician-K dominated by scattering from the UAV arms and propellers. To capture these observed trends, we model the Rician-K variations using Gaussian functions, extending our previous work [11]:

$$g(\chi_{AG}) = a_1 \exp\left(-\frac{(\chi_{AG} - b_1)^2}{2c_1^2}\right), \tag{13}$$

$$g(\theta) = a_2 \exp\left(-\frac{(\theta - b_2)^2}{2c_2^2}\right), \tag{14}$$

where χ_{AG} denotes the UAV altitude, θ the elevation angle, and the parameters a_1, b_1, c_1 and a_2, b_2, c_2 represent the amplitude, centroid, and width of the Gaussian peaks, respectively, determined by antenna placement and environmental conditions. The Gaussian modeling provides a smooth and flexible approximation of both monotonic and non-monotonic Rician-K trends, effectively capturing the combined effects of UAV altitude, elevation angle, antenna configuration, and environment, as further validated by the measurement results presented in Section V. The Gaussian form reflects the dominance of a peak LoS contribution at intermediate geometries, with reduced dominance at both low and high altitudes due to multipath and geometric spreading.

C. AIR2UG SIGNAL MODEL

The Air2UG channel signal model is defined by incorporating both path loss and small-scale fading effects. Let $y_m(t)$ denote the signal received at the UG node m from the UAV located at a specific position at time t, in Fig. 1. The received signal $y_m(t)$ can then be expressed as:

$$y_m(t) = u_m(t)h_m(t) + n(t),\ \forall m = \{1, \cdots, M\} \tag{15}$$

where M is the total number of UG nodes, $u_m(t)$ is the transmitted signal, $n(t)$ is the AWGN noise,

$$h_m(t) = \sqrt{\zeta_m(t)}g_m(t) \tag{16}$$

is the total channel between UAV and the UG node in Fig. 1 where $\zeta_m(t)$ represents the attenuation due to the signal path distances (AG and UG) and soil properties, and $g_m(t)$ refers to the small-scale fading. Moreover, $g_m(t)$ is modeled with a Rician fading as $g_m(t) = \sqrt{\frac{K_m}{K_m+1}}g + \sqrt{\frac{1}{K_m+1}}\hat{g}$, where g denotes the direct signal path component with $|g| = 1$, $\hat{g}$ represents the reflected/scattered signal paths components which is a circularly symmetric complex Gaussian random variable with zero mean and unit variance, and K_m denotes the Rician-K. Also, $\zeta_m(t)$ can be calculated from (8) and (9) as:

$$\begin{aligned}\zeta_m(t) =& \frac{2.93 \times 10^{11}\gamma_m(t)G_{AG}G_{UG}(1 - 10^{RL_{UG}/10})}{d^{\eta}_{AG_m}(t)\beta^2_m d^2_{UG_m}(t)f^2} \times \\ & \frac{\cos(\theta_m(t))\sqrt{e'_{s_m} - \sin(\theta_m(t))^2}}{(\cos(\theta_m(t)) + \sqrt{e'_{s_m} - \sin(\theta_m(t))^2})^2},\end{aligned} \tag{17}$$

where

$$\begin{aligned}\gamma_m(t) =& 10^{-0.869\alpha_m d_{UG_m}(t)} \times \\ & 10^{3.255\cos(1.185\theta_m(t)) + 3.255w\sin(1.185\theta_m(t))}.\end{aligned} \tag{18}$$

Moreover, we observe that both the path loss and the small-scale fading effects of the Air2UG channel exhibit similar characteristics in the uplink and downlink. Therefore, the uplink signal transmitted from the UG node and received by the UAV can be modeled using the same expression as in (15).

IV. IN-FIELD EXPERIMENT SETUP

The measurement system used for in-field outdoor measurements is first presented in this section. Then, we present the measurement campaign and location-specific information, such as the characteristics of the soil and wireless propagation environment.

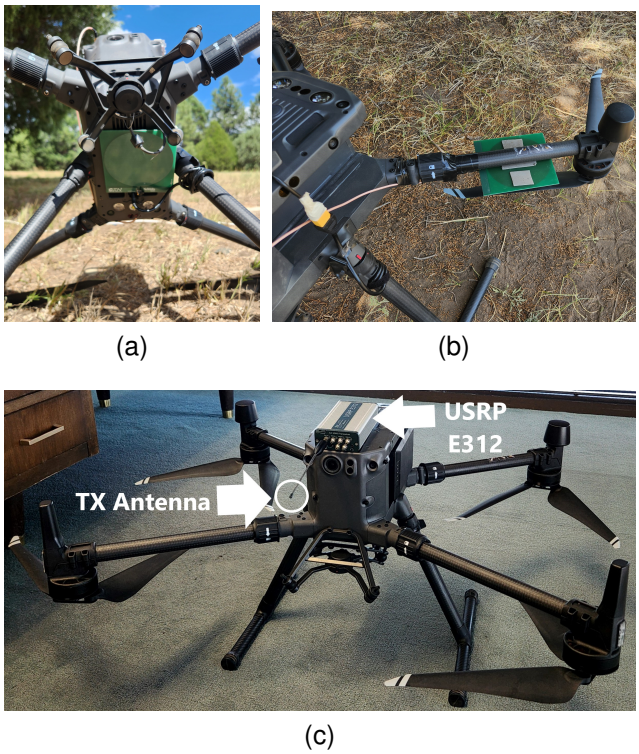

FIGURE 2: Custom patch antenna on a UAV: (a) body (bottom) and (b) arm; (c) tri-band antenna with USRP E312 on a UAV used in [11]

A. AIR-TO-UNDERGROUND MEASUREMENT SYSTEM

We utilize a similar measurement system that we design in [11]. The system comprises 2 USRP E312, where one of the USRPs is mounted on the commercial UAV and the other USRP is connected to two UG antennas through 0.5 m cables that are buried at depths of 0.1 m and 0.2 m. For the downlink measurements, the UAV-mounted USRP transmits a continuous sinusoidal signal that is captured at two UG antennas simultaneously. While in the uplink, the 0.1 m-depth antenna first transmits a continuous sinusoidal signal that is captured by the UAV, followed by the 0.2 m-depth antenna. In this way, uplink measurement data is captured in two separate flights. The transmitter and receiver scripts are implemented in Python via GNU Radio libraries and transferred to the USRPs. Before each flight, the Python scripts are executed for a limited flight time in the USRPs via a shell script that also logs the start and stop times of the scripts for data synchronization. Note that the receiver captures the IQ samples in a file continuously for the fixed duration of the UAV flight time, which is then post-processed in MATLAB to generate results.

Moreover, we employ a matched wideband patch antenna at both UAV and UG nodes. The antenna has a strong radiation pattern on a single side of the plane, which makes it suitable for the UAV-based sensor data collection application. Also, the patch antenna can easily be designed and merged with the UAV body. However, in previous work, it has been reported that the antenna placement on the UAV body has a significant impact on the antenna radiation characteristics [31]. Therefore, to analyze such an impact on communication between UAV and UG nodes, we mount the antenna on the UAV body frame at two distinct positions that are shown in Fig. 2a and Fig. 2b and conduct wireless propagation measurements in each case separately. For comparison, the UAV measurement system employed in our previous work [11] is shown in Figure 2c, where a triband antenna is directly connected to a USRP E312 for transmission. Note that in the remainder of the paper, measurements with the antenna mounted on the bottom plate of the UAV are referred to as "Bottom" and measurements with the antenna mounted on the arm of the UAV are referred to as "Arm". Table 1 lists the remaining measurement system parameters.

TABLE 1: Measurement system parameters

Parameter	Value
Carrier Frequency	1.241 GHz
TX Power	15.5 dBm
Sampling rate	300K samples/seconds
TX and RX Antenna	Custom wide-band [32]
Transmit signal	Sine wave
UAV	DJI Matrice 300 RTK

B. IN-FIELD EXPERIMENTATION PLAN

We aim to measure the radio propagation characteristics in the channel at various 3D positions of the UAV. In that context, measurements are taken in two distinct topologies, which are shown in Fig. 3a and 3b, wherein both topologies, two antennas are buried in the soil at 0.1 m and 0.2 m depths with a horizontal separation of 0.5 m which infers typical moisture sensor deployments. In the first topology, the UAV varies its altitude from 5 m to 29 m while flying straight overhead the 0.2 m-depth antenna and hovering for 20 seconds every 3 meters through an automated flight plan. In the second topology, the UAV flies at a fixed distance of 21 meters from the 0.2 m antenna and varies the elevation angle between 0 degrees and 75 degrees while hovering every 15 degrees for 20 seconds. Since the receiver captures the IQ data continuously, the recorded UAV flight data is utilized in the post-processing along with the receiver script timestamps to extract the received IQ data of each hovering waypoint from the receiver data file. Moreover, the aerial view of the measurement location is shown in Fig. 3c, wherein a pair of medium-height trees neighbor the UG antennas on the north side, the south side is wide open, the west side has two adobe structure small homes, and the east side also has multiple medium-height trees. For comparative analysis, we also include empirical results from experiments in our previous work in [11], which were obtained at a different location enclosed in a wooden fort structure with a sky-open top and high trees in the vicinity, as shown in Fig. 3d.

To measure soil moisture, two Watermark sensors [33] are buried alongside the UG antennas as shown in Fig. 3c (top). These sensors measure soil water tension in centibars (cB),

This article has been accepted for publication in IEEE Access. This is the author's version which has not been fully edited and
content may change prior to final publication. Citation information: DOI 10.1109/ACCESS.2026.3697971

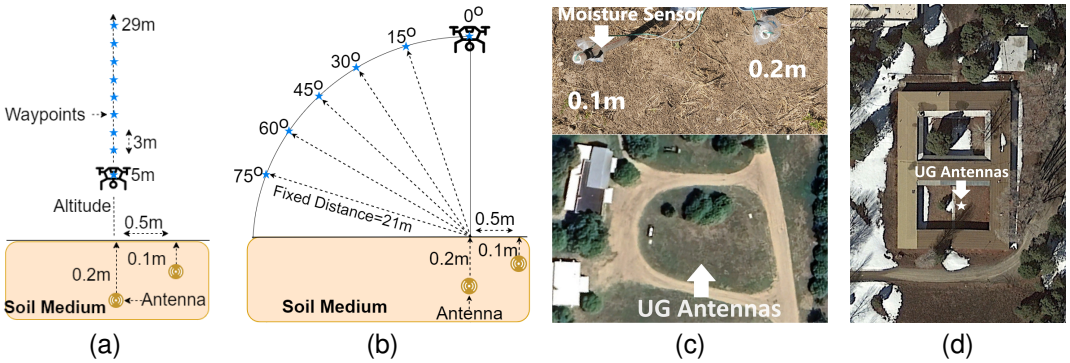

FIGURE 3: Measurement topologies and field setup: (a) UAV flight path with varying altitudes, (b) UAV trajectory with different elevation angles, (c) aerial view of the site with UG antenna placements, and (d) aerial view of the site in [11].

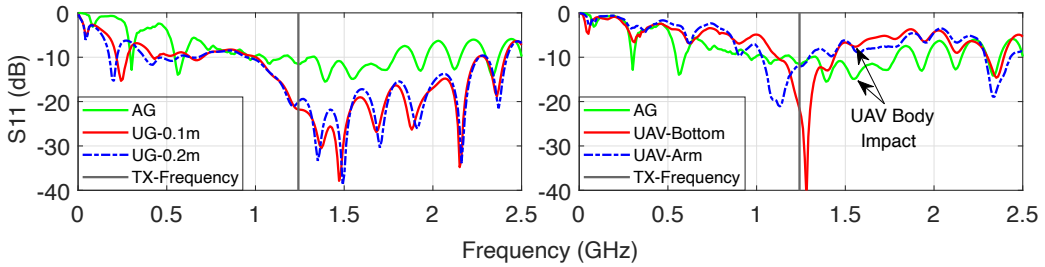

FIGURE 4: S_{11} measurements for AG, UG, and UAV body.

which has an inverse relationship with soil moisture. Since soil moisture has a significant impact on the channel in UG communication, all measurements were conducted at two soil moisture levels: 7 centibars (cB) for wet soil and 239 cB for dry soil. Moreover, the soil texture at the measurement location is sandy clay loam at all depths. The bulk density of the soil and its textural composition change marginally with depth. At 0.1 m, the soil contains 56 percent sand, 23 percent silt, and 21 percent clay. Similarly, at 0.2 m, the percentages are 56, 20, and 24. The bulk density values at depths of 0.1 m, and 0.2 m are 0.58 gr/cm^3, and 0.89 gr/cm^3, respectively. Also, the measurement sites in Fig. 3c and Fig. 3d are both located on the SMU-in-Taos campus in Taos, New Mexico.

V. INFIELD CHARACTERIZATION OF THE AIR2UG AND UG2AIR CHANNELS

In this section, we characterize the path loss and small-scale fading in Air2UG and UG2Air channels through outdoor measurements. In particular, the impact of the UAV's antenna position, soil depth, and soil moisture on the channels is studied. We also examine the impact of the UAV body on the wide-band antenna's reflection coefficient, denoted by the S_{11} parameter.

A. ANTENNA RETURN LOSS

The antenna S_{11} is measured through a vector network analyzer in AG, UG (dry soil), and UAV-mounted settings. The measured S_{11} values are presented in Fig. 4. Note that a –10 dB antenna reflection coefficient indicates that 90% of the transmitted power is transferred to the antenna to be radiated. Therefore, the S_{11} threshold of -10 dB is taken into account when comparing the outcomes across all frequencies. It can be seen that the S_{11} changes significantly between AG and UG cases, which is also seen in the prior work [11]. The S_{11} varies marginally between the soil depths, and at the transmission frequency, the S_{11} is at approximately -20 dB, which infers that the antenna is suitable for communication when buried in the UG. The impact of soil moisture on the antenna properties in the UG can be found in [34]. Moreover, by comparing the results of AG and UAV body cases, it is evident that the UAV body has a significant impact on the antenna characteristics. For instance, the S_{11} values at most frequencies between 1.4 GHz and 2.2 GHz are 1.7 dB – 7.5 dB higher than the AG results, causing the S_{11} to rise above the –10 dB threshold. This increase indicates reduced impedance matching and greater signal reflection. Similarly, at 300 MHz and 570 MHz, the S_{11} increases by 9.5 dB – 11.1 dB, further exceeding the –10 dB threshold and highlighting additional degradation in matching performance.

We also found that there are variations in S_{11} with respect to the placement of the antenna on the bottom versus the arm of the UAV. There are a few frequencies that are more suitable for transmission when the antenna is placed on the arm versus the bottom of the UAV, and vice versa. For example, the S_{11} at the 1.07 GHz frequency is 2.1 dB above the –10 dB threshold in UAV Bottom results while in the UAV arm results, the S_{11} is 7 dB below the threshold level at the same frequency. In contrast, the S_{11} at 1.32 GHz

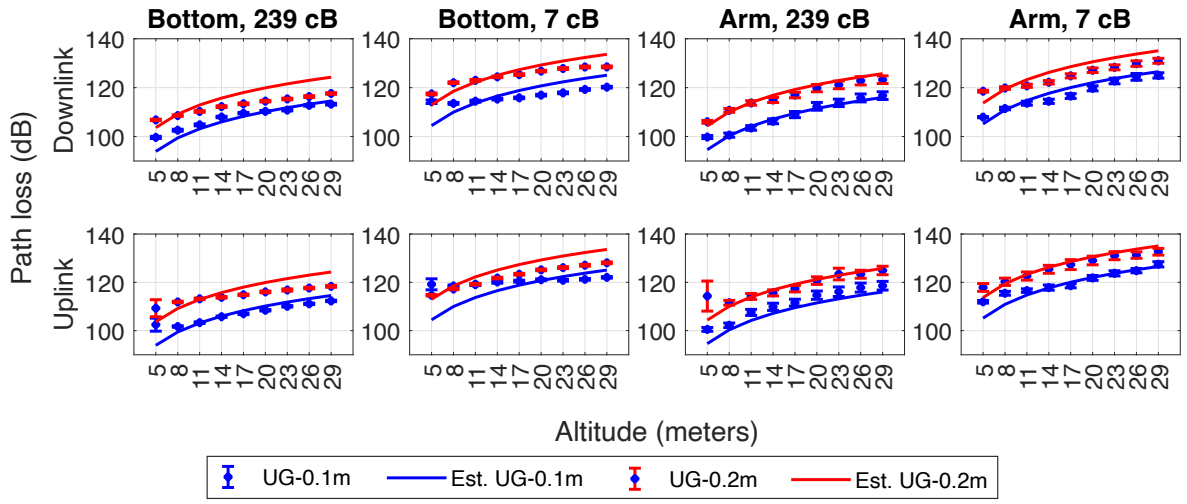

FIGURE 5: Measured and estimated path loss at various UAV altitudes

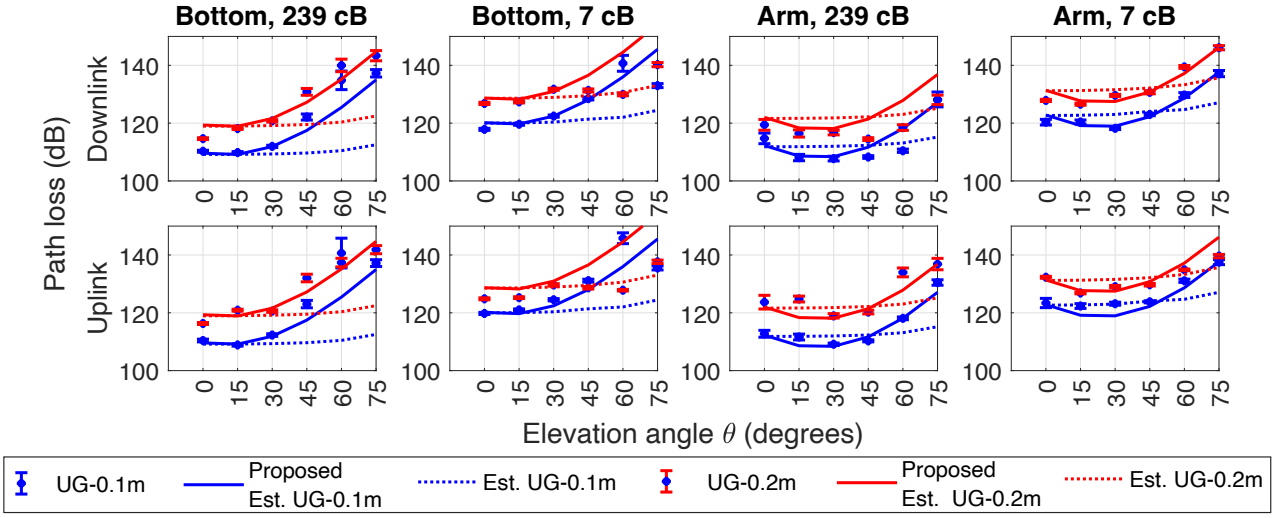

FIGURE 6: Measured and estimated path loss at various UAV elevation angles

frequency is above the –10 dB threshold by 2.3 dB in UAV Arm results while in UAV Bottom results, the S_{11} is 5.8 dB below the threshold level at the same frequency. Therefore, it is important to consider the impact of the UAV body on the antenna characteristics before the aerial network deployment.

B. AIR-TO-UNDERGROUND PATH LOSS CHARACTERIZATION

The path loss values in the measurements are calculated from received signal IQ samples for each waypoint in the measurement topologies. The measured path loss values in Air2UG and UG2Air channels at multiple UAV altitudes for various soil depths, soil moisture, and UAV antenna positions are shown in Fig. 5. It can be seen that, while the path loss varies considerably between several cases, it always rises with UAV altitude. The path loss comparison between uplink and downlink cases shows similar performance, and on average, the difference is only 2.2 dB, where the variation is mainly found in the measurements with the bottom antenna, which infers approximately identical large-scale performance in the bi-directional channels. The impact of an increase in soil moisture from 239 cB to 7 cB shows that the path loss with the bottom antenna increases by 10.91 dB and 9.9 dB at 0.1 m and 0.2 m depths, and with the arm antenna, it increases by 8.75 dB and 8.05 dB at 0.1 m and 0.2 m depths, respectively. Comparably, the effect of increasing the depth from 0.1 m to 0.2 m shows that the path loss increases by 6.28 dB and 5.98 dB at 239 cB and 7 cB for the bottom antenna and by 7.67 dB and 6.98 dB at 239 cB and 7 cB for the arm antenna, respectively. The variation with respect to the UAV antenna position is also seen in the results. The main observation is that the slope of change in path loss values with respect to the altitude is lower in the bottom antenna compared to the arm antenna. Therefore, at higher altitudes, the bottom

TABLE 2: Soil parameters [11]

Parameter	Value
$\rho_s(gr/cm^3)$	2.65
$\rho_b(gr/cm^3)$	0.58 (0.1m), 0.89 (0.2m)
m_v	0.15, 0.35
S	0.56,
C	0.21 (0.1m), 0.24 (0.2m)
ϵ_o, $\epsilon_{fw}^{'}$, μ, ϵ_{w0}, $\epsilon_{w\infty}$	55.26, 79.71, 6, 80.1, 4.9
$\epsilon_{fw}^{''}$	25.31 (0.1m), 40.27 (0.2m)
δ_{eff}	0.08 (0.1m), 0.17 (0.2m)
$2\pi\tau_w(s)$	0.58×10^{-10}

antenna provides approximately 9 dB lower path loss values than the arm antenna, which is beneficial in improving the communication range. This is because the overall body of the UAV serves as a reflector and directs radio waves to or from the bottom plate of the UAV such that the signal strength in the main lobe of the antenna increases compared to the side lobes.

Next, the path loss values are estimated at multiple UAV altitudes using the model in (1) and the area-specific soil parameters provided in Table 2. The estimated results are also shown in Fig. 5. As can be observed, overall, the path loss model captures the empirical data with minimal errors. The RMSE values between the measured and estimated results range between 1.86 dB – 4.38 dB in the downlink and 2.01 dB – 6.70 dB in the uplink, where the measurements taken with the bottom antenna, particularly at higher altitudes, are where the majority of the large estimation errors are found.

As a reference for comparison, we present the measured and estimated downlink path loss results of our previous study [11], obtained at various altitudes using the measurement topology depicted in Fig. 3a and corresponding to the location shown in Fig. 3d. The results obtained under saturated wet soil conditions are presented in Fig. 7a. The results indicate an average increase of 5.9 dB in path loss as the antenna depth changes from 0.1 m to 0.2 m. Furthermore, the path loss is observed to increase with altitude. In addition, the fading observed in the path loss measurements (represented by the error bars) varies with altitude. An increase in fading is observed at higher altitudes, which is reflected similarly in the Arm antenna path loss results shown in Fig. 5. The estimated path loss results, calculated using (1), show good agreement with the measured values, resulting in RMSE of 3.8 dB and 1.6 dB at antenna depths of 0.1 b and 0.2 m, respectively.

The impact of elevation angle on the path loss in Air2UG and UG2Air channels is shown in Fig. 6. It can be seen that the measured path loss values change significantly between the 0-degree and 75-degree elevation angles in both the uplink and downlink. We observed that the variation in path loss with elevation angle is significantly dependent on the antenna position on the UAV. In the bottom antenna results, the trend shows that the path loss mainly increases with the increase in the elevation angle, with some exceptions found in the results at 239 cB moisture and 0.1 m-depth, where the 15-degree elevation angle provides similar or slightly lower path loss values than the 0-degree elevation angle. Accordingly, on average, the path loss increases by 29.14 dB between 0 and 75 degrees and increases by 25.16 dB from 239 cB to 7 cB. Contrary to this, the path loss first decreases and then increases with the elevation angle in the arm antenna results, where the elevation angles with the lowest path loss values are mostly found at 30 degrees or 45 degrees, which implies that the UAV position directly above the UG antennas does not provide the optimal performance. Therefore, choosing the angle with the lowest path loss value improves the performance by 18.32 dB and 16.6 dB at 239 cB and 7 cB, respectively, when compared with the worst UAV position with 75 75-degree angle.

The path loss is estimated at various elevation angles using the model in (1), where we utilize refraction loss given in (4) in both uplink and downlink results. The estimated results are also shown in Fig. 6 with the dotted lines. The estimated results in most cases show the inability of the path loss model in (1) to represent the empirical measurements. This is because the refraction loss in (4) is a monotonically increasing function in elevation angle, while there are two measurement trends found in the bottom and arm antenna cases that we discussed before. Also, the estimated path loss increases by less than 1 dB per 15-degree increment between 0 degrees and 60 degrees elevation angles. At 75 degrees, however, the increase reaches approximately 5 dB, which remains substantially lower than the variation observed in the measured data. The higher estimation errors are mostly found at elevation angles greater than 30 degrees, and it seems that there are additional losses in the channel, which are more significant at large elevation angles. The performance of the model is quantified using the RMSE values. The average RMSE in the bottom antenna results with 239 cB soil moisture is 15.98 dB and 12.24 dB at 0.1 m and 0.2 m depths, and with 7 cB soil moisture, it is 10.25 dB and 3.20 dB at 0.1 m and 0.2 m depths, respectively. Similarly, the RMSE of the arm antenna results is 6.48 dB and 5.90 dB at 0.1 m and 0.2 m depths with 239 cB soil moisture, and 5.09 dB and 4.23 dB at 0.1 m and 0.2 m depths with 7 cB soil moisture, respectively. While the path loss model shows limited performance in several cases, it was able to capture some scenarios with considerably lower errors, particularly at shallower depths or under lower soil moisture conditions.

To show the effectiveness of the new Air2UG path loss model in (9), we estimate the path loss at various elevation angles, soil depth, soil moisture, and UAV antenna positions and present the results in Fig. 6 with solid lines. The empirically determined parameters in (10) are $k_1 = 32.55$, $k_2 = k_4 = 1.84$, and k_3 is 0.20 and 0.52 in the Bottom and Arm antenna results, respectively. It can be seen that the path loss model captures the empirical results well in nearly all the measurement cases, compared to the model in (1). The RMSE value in the Bottom antenna results with 239 cB soil moisture is 5.53 dB and 3.04 dB at 0.1 m and 0.2 m depths, and with 7 cB soil moisture, it is 5.74 dB and

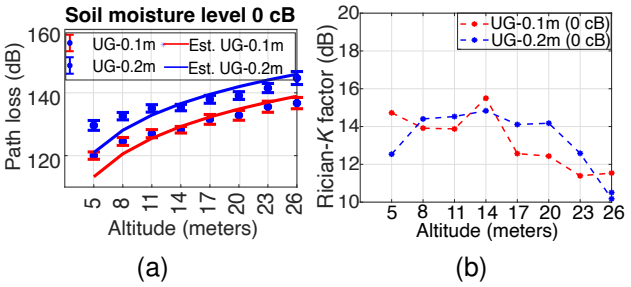

FIGURE 7: Path loss and Rician K-factor versus altitude at location in Fig. 3d, from [11].

8.52 dB at 0.1 m and 0.2 m depths, respectively. Similarly, the RMSE value in the Arm antenna results with 239 cB soil moisture is 1.96 dB and 4.93 dB at 0.1 m and 0.2 m depths, and with 7 cB soil moisture, it is 1.88 dB and 2.45 dB at 0.1 m and 0.2 m depths, respectively. Overall, the new model consistently provides lower estimation errors across a wide range of environmental conditions and antenna configurations, offering improved reliability for Air2UG and UG2Air channel characterization.

C. AIR-TO-UNDERGROUND SMALL-SCALE FADING CHARACTERIZATION

The small-scale fading in the Air2UG and UG2Air channels is modeled using the received signal magnitude results acquired by post-processing the received IQ samples. In [11], we model the small-scale fading in the Air2UG channel using the Rician distribution and verify it with a confidence-based equality test. Therefore, we model the UG2Air channel as a Rician fading channel and show the validity by comparing the empirical CDF and fitted Rician CDF in the uplink measurements. The Rician distribution function is fitted to the measured signal for each measurement case using the maximum likelihood estimation. To evaluate the overall goodness of fit, we employ the Kolmogorov-Smirnov (KS) test, a widely used non-parametric method for assessing whether two observed sets of samples originate from the same distribution. The KS test between the Rician fit and the empirical data does not reject the null hypothesis at the 10% significance level, indicating statistical consistency between the fitted and empirical distributions.

The empirical and fitted Rician CDF of the received signal at the UAV (bottom antenna) with 5 m altitude for a signal transmitted from the UG antenna at 0.1 m depth with soil moisture 239 cB is shown in Fig. 8. It can be seen that the Rician CDF closely follows the empirical data. To evaluate the quality of the fit, we adopt the Weighted Mean Relative Difference (WMRD) as an error vector norm technique that measures the difference between the fitted model and the actual data. The WMRD is computed between the empirical

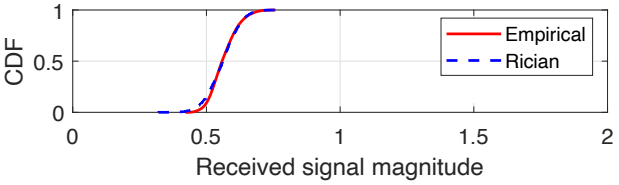

FIGURE 8: Empirical CDF of the received signal magnitude, and corresponding estimated Rician and Bivariate CDFs.

and fitted CDFs as [35]:

$$\text{WMRD} = \frac{\sum_{i=1}^{N} |y_{\text{e}}(x_i) - y_{\text{f}}(x_i)|}{\sum_{i=1}^{N} (y_{\text{e}}(x_i) + y_{\text{f}}(x_i)) \times 0.5}, \qquad (19)$$

where $y_{\text{e}}(x_i)$ and $y_{\text{f}}(x_i)$ are the empirical and fitted CDF values at sample x_i, and N is the total number of samples. For the CDF shown in Fig. 8, the WMRD is 0.10, indicating that the Rician model provides a close and meaningful fit to the measured data.

The Rician-K values are calculated from the estimated Rician distribution parameters. The Rician-K values with respect to altitude at various soil depths, moisture levels, and UAV antenna positions are shown in Fig. 9. The Rician-K parameter is dependent on the altitude, and the antenna position on the UAV has a significant impact on the variation. Overall, the bottom antenna results show that the Rician-K in both uplink and downlink initially increases and then decreases with altitude, whereas it only decreases with altitude in the arm antenna results. Also, on average, the Rician-K value in the bottom antenna is approximately 9 dB higher than the arm antenna, which means that the overall body of the UAV positively influences the signal propagation to or from the bottom antenna position of the UAV, such that the antenna observes weaker signal reflections or a stronger direct signal path. This indicates that even slight variations in the UAV antenna position can reduce fading-related errors, enhance the reliability of data collection from UG sensors, and enable communication from deeper soil layers or over longer UAV–sensor distances. Furthermore, an increase in soil moisture content from 239 cB to 8 cB increases the Rician-K value by 3.27 dB with the arm antenna, but the impact is insignificant in the measurements with the bottom antenna. In most cases, the overall influence of increasing burial depth has a negligible effect on Rician-K values, although some noticeable variations are observed at lower altitudes. In our previous work [11], the variation of the Rician-K factor with altitude was also observed, as presented in Fig. 7b. Specifically, Rician-K increases with altitude up to a point and then decreases, a pattern that closely aligns with the results obtained with the bottom antenna in this work (Fig. 9).

The impact of elevation angle on the Rician-K factor in Air2UG and UG2Air channels is shown in Fig. 10. It can be seen that in all cases, the Rician-K value is significantly dependent on the elevation angle. However, the variation in the values is dependent on the antenna position on the UAV, similar to the path loss results. The Rician-K values

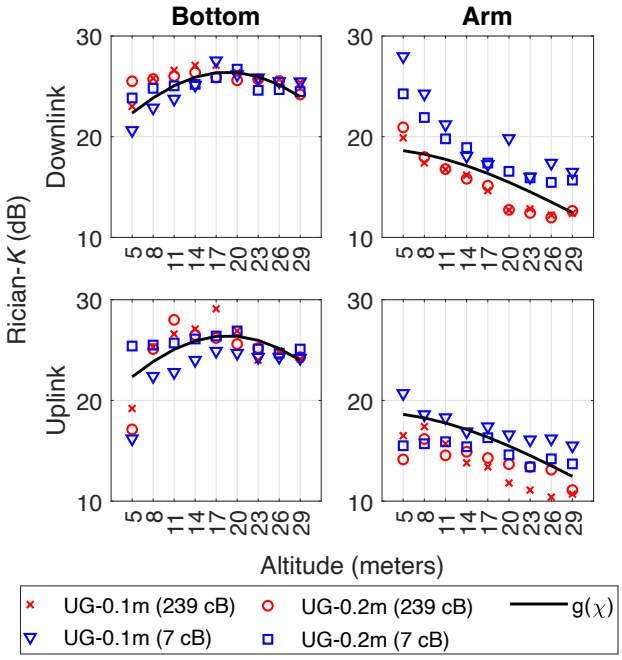

FIGURE 9: Rician-K versus altitudes.

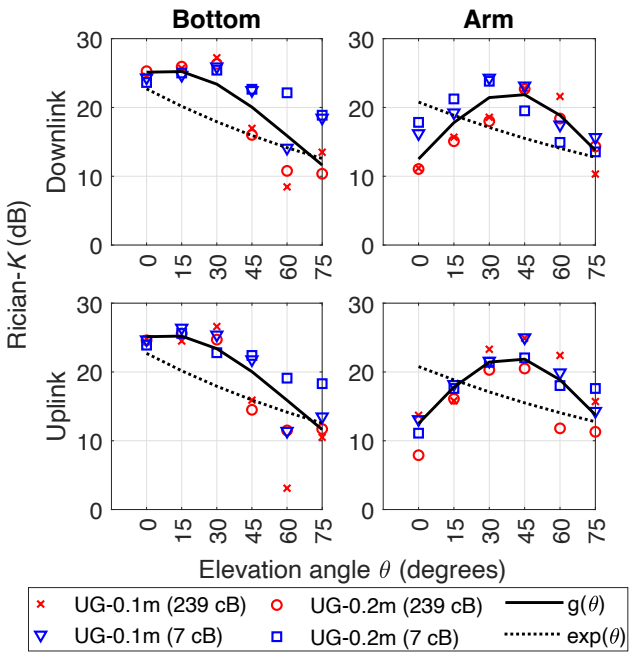

FIGURE 10: Rician-K versus elevation angles.

first increase and then decrease with the elevation angle. The elevation angles with the highest Rician-K values are 15 degrees – 30 degrees in the bottom antenna and 30 degrees – 45 degrees in the arm antenna. An important observation is that choosing the appropriate elevation angles for communication can provide comparable Rician-K performance between bottom and arm antenna cases, such that the impact of UAV antenna position on Rician-K is minimized. Also, even at 75-degree elevation angle (close to the ground), the Rician-K value remains approximately 10 dB, indicating that the radio signals reaching the ground-soil interface are not completely reflected and there is a signal wave propagating along the ground surface (i.e., lateral wave) that is reaching the UG node in the downlink and the UAV in the uplink. Note that the authors in [30] demonstrated that the Rician-K factor in A2G communication decreases with elevation angle. This variation is modeled by the exponential function in (12), as originally proposed in [19]. We now estimate the Rician-K variation with respect to the elevation angle in Air2UG and UG2Air channels using the model in (12). The estimated results are also shown in Fig. 10 with dotted lines, where the empirically determined model parameters A_1 and A_2 in (12) are 12.571 and 0.0079, respectively. The comparisons between empirical and estimated results show that the model in (12) is incapable of representing the Rician-K values in the Air2UG and UG2Air channels due to large estimation errors. This is because the estimated Rician-K values from (12) monotonically decrease with elevation angle and vary between the maximum and minimum Rician-K values in the environment, which is not the general trend in the empirical measurements. The RMSE values range between 5.42 dB and 6.94 dB in the arm antenna measurements, while in the bottom antenna, they range between 4.4 dB and 8.2 dB. Note that the empirical results trends in Fig. 9 and Fig. 10 can be captured by a Gaussian function when $K >> 1$.

Accordingly, we fitted the functions $g(\chi_{AG})$ in (13) and $g(\theta)$ in (14) on the empirical Rician-K values from Fig. 9 and Fig. 10 using the maximum likelihood estimation, respectively. The estimated results are also shown in Fig. 9 and 10. The RMSE of the fitted $g(\chi_{AG})$ function in Fig. 9 varies between 2.86 dB – 4.38 dB, with the substantial estimation errors mostly found in the 239 cB soil moisture and 0.2 m depth results due to the limited variation of Rician-K with altitude. In the Bottom and Arm antenna findings, the fitted Gaussian function parameters $\{a_1, b_1, c_1\}$ are {26.42, 18.63, 23.52} and {18.85, 5, 31.86}. The RMSE of the fitted $g(\theta)$ function in Fig. 10 ranges between 2.1 dB and 6.1 dB in the Bottom antenna results, while it ranges between 1.89 dB and 3.14 dB in the Arm antenna results. The corresponding fitted Gaussian function parameters $\{a_2, b_2, c_2\}$ are {25.42, 8.17, 53.42} and {22.13, 39.24, 36.73} in the Bottom and Arm antenna results, respectively. The errors in the estimation suggest that the UAV has lower Rician-K estimation errors at small elevation angles and mid-range altitudes, highlighting the benefit of near-vertical positioning above UG sensors.

Comparing the Rician-K estimated results from exponen-

tial function and $g(\theta)$ function in Fig. 10 shows that the $g(\theta)$ achieves an average estimation error reduction of approximately 3 dB, translating to a 47% improvement over the exponential function. The improvement in Rician-K estimation reduces channel uncertainty, improving link reliability and enabling more efficient and robust communications between UAV and UG sensor nodes. Hence, it can be concluded that the Gaussian functions in (13) and (14) can be utilized to estimate Rician-K for various altitude and elevation angles in Air2UG and UG2Air channels.

VI. UAV-COLLECT: ENERGY EFFICIENT DATA COLLECTION IN UAV-IOUT

In this section, we consider an application of our findings in the prior section for optimal data collection in the IoUT. For this purpose, we first present the system model of the network and cast the energy minimization problem. Accordingly, the solution to the problem, *UAV-Collect* algorithm, is presented. Finally, numerical results are presented to show the effectiveness of *UAV-Collect* and models.

A. EFFICIENT DATA COLLECTION FOR UAV-IOUT SYSTEM MODEL

We consider a UAV-enabled IoUT, where a UAV is deployed for mission time $T_{\max}$, to collect data from M battery-operated underground sensors (SNs) that are buried in an agricultural field at various soil depths for soil monitoring. The location of each SN is defined by $(\mathbf{w}_m, \chi_{UG_m}), \forall m \in \mathcal{M} = \{1, \ldots, M\}$, where $\mathbf{w}_m = [w_m^x, w_m^y]^T \in \mathbb{R}^{2\times 1}$ corresponds to the horizontal location coordinates of the SNs. The 3D trajectory of the UAV is defined by $\mathbf{q}(t) = [q^x(t), q^y(t)]^T$ and $\chi_{AG}(t)$, denoting the horizontal location and altitude of the UAV at time instant t, respectively. The UAV's initial or takeoff position is defined by $(\mathbf{q}^I, \chi_{AG}{}^I)$ with $\mathbf{q}^I = [q^{x^I}, q^{y^I}]^T \in \mathbb{R}^{2\times 1}$ corresponding to the horizontal coordinates and $\chi_{AG}{}^I$ is the altitude. The UAV lands at the respective takeoff position $\mathbf{q}^I$ after completing the sensor data collection task. Accordingly, the channel between the UAV and SN m is defined by (16)–(18), where the AG distance d_{AG_m} at time t can be written as

$$d_{AG_m}(t) = \sqrt{\|\mathbf{q}(t) - \mathbf{w}_m\|^2 + \chi_{AG}(t)^2} \tag{20}$$

During the flight mission, the UAV adopts the TDMA protocol to collect data from SNs, with each SN transmitting data after being woken up by the UAV within the scheduled time frame. In this manner, the SNs conserve energy and only consume it when triggered by the UAV. Further, we define a binary variable $x_m(t) \in \{0, 1\}$ for communication scheduling, where $x_m(t) = 1$ shows that SN m is scheduled or woken up by UAV for data transmission at time instant t and stays in sleep mode otherwise. Due to the utilization of the TDMA protocol, only a single SN is woken up for data collection by a UAV at any time instant t. We also assume that each SN is only served once during the flight mission. As a result, we have the following scheduling constraints:

$$\sum_{m=1}^{M} x_m(t) \leq 1, \forall t \tag{21}$$

Let $p_m(t)$ denote the uplink transmit power of the SN m at time t, which should satisfy the power constraint: $0 \leq p_m(t) \leq P_{\max}$, where $P_{\max}$ is the peak transmit power of the SNs. Then, assuming that SN m is scheduled for transmission at time instant t, the achievable uplink rate can be written as:

$$C_m(t) = W \log_2 \left(1 + \frac{p_m(t)|h_m(t)|^2}{W N_o}\right) \tag{22}$$

where W is the bandwidth and N_o is the noise power. Note that $C_m(t)$ is not exactly known before the flight because $h_m(t)$ is dependent on the undetermined moisture content of the soil at each SN as well as the instantaneous channels that change with the movement of the UAV. Therefore, one of the solutions is to consider an adaptive transmission rate scheme that is upper-bounded by the worst-case channel condition of the saturated wet soil with 0 cB moisture value. However, in the case when the soil condition around most of the sensors is dry. The UAV and SN will be consuming more energy to exchange the data bits, while the SNs could transmit at a higher transmission rate to conserve the energy consumption utilized for transmission. To solve this issue, we adopt an adaptive transmission rate scheme, where the UAV determines the rate $R_m(t)$ in the flight by estimating the soil moisture content of the SNs through prior spatial moisture correlation information among the SN locations. More specifically, the UAV flies to the first SN, collects the data with a transmission rate corresponding to the worst channel case of saturated wet soil condition, processes the collected data to estimate the moisture content of the first SN, estimates the moisture content of the remaining SNs through spatial correlation information, and select the transmission rate for remaining SNs that correspond to the estimated moisture content information. Note that the soil moisture over an area is highly spatio-temporally correlated, which depends on the rainfall and vegetation in a particular area [36]. The spatial correlation in the soil moisture content between two SNs is modeled as $\rho_s(i, j) = (1 + 0.25\rho_R d_{i,j}) \exp(-0.5\rho_R d_{i,j})$ [36], [37], where $d_{i,j}$ is the distance between SN i and SN j, and ρ_R is the mean rain cell radius. Therefore, provided the moisture content of the first SN, the moisture content of the rest of the SNs can be estimated using ρ_s. Following, the outage probability that the UAV will not successfully receive the transmitted data from SN m at time t is given as:

$$\mathcal{P}_m(t) = \mathbb{P}(C_m(t) < R_m(t)) \tag{23}$$

$$= \mathbb{P}\Big(|g_m(t)|^2 < \underbrace{\frac{W N_o (2^{R_m(t)/W} - 1}{\zeta_m(t) p_m(t)}}_{r}\Big) = F(r) \tag{24}$$

where $F(r)$ denotes the CDF of $|g_m(t)|^2$, and for Rician fading, it can be expressed as $F(r) = 1 - Q\left(\sqrt{2K_m}, \sqrt{2(K_m+1)r}\right)$, where Q is the Marcum-Q function. To ensure that the uplink data is reliably received by the UAV, $R_m(t)$ should be selected such that $\mathcal{P}_m(t) = \epsilon$, where ϵ is the maximum tolerable outage probability which practically ranges between 0 and 0.1 [19]. The outage-aware transmission rate can be written as:

$$R_m(t) = W \log_2 \left(1 + \frac{E[p_m(t)]|h_m(t)|^2 f_m(t)}{W N_o}\right) \quad (25)$$

where $f_m(t) = F^{-1}(\epsilon)$ is defined as effective fading power in the prior work [19]. When $F(1) < \epsilon$, $f_m(t) = 1$. Also, $f_m(t)$ depends on the Rician-K that changes with the altitude and elevation angle between UAV and SN. In prior works, $f_m(t)$ is only modeled for elevation angles [19], [38]. Due to the lack of an explicit form of the inverse Marcum-Q function, effective fading power f is approximated by $f = \frac{e^2}{2(K+1)}$ in [19], where e is defined as:

$$e = \begin{cases} \sqrt{-2\ln(1-\epsilon)}\, e^{K/2}, & K \le K_{th}^2/2 \\ \sqrt{2K} + \frac{1}{2Q^{-1}(\epsilon)} \ln\left(\frac{\sqrt{2K}}{\sqrt{2K} - Q^{-1}(\epsilon)}\right) & \\ -Q^{-1}(\epsilon), & K > K_{th}^2/2 \end{cases}$$

in which Q^{-1} is the inverse Q-function and K_{th} is the intersection of sub functions at $\sqrt{2K} > Q^{-1}(\epsilon)$. The above formulation of f is still complicated. Thus, in [19], f as a function of θ_m for A2G channels is approximated by a logistic model, where the approximation is based on the exponential relationship of the Rician K factor concerning θ_m in (12), which did not fit our empirical results in Fig. 10, and the approximation concerning the altitude is not defined. Therefore, we approximate f in the UG2Air and Air2UG channels for θ_m and χ_{AG} separately using linear regression. We first generate the numerical values of f for θ_m between 0 degrees and 75 degrees and χ_{AG} between 5 m and 29 m using (13) and (14) with Gaussian parameters from both UAV antenna cases. Then we analyze the variation of f for θ_m and χ_{AG}, as shown in Fig. 11. We find that f varies similarly to the Gaussian estimated Rician-K values. We test fitting a Gaussian function to the numerical results as shown in Fig. 11 and find that the Gaussian can be utilized to approximate f with RMSE less than 0.049. Therefore, we approximate f with respect to χ_{AGm} and θ_m as:

$$f_m^{\chi_{AG}}(t) \approx A_1 \exp\left(-\frac{(\chi_{AGm}(t) - B_1)^2}{2(C_1)^2}\right), \quad (26)$$

$$f_m^{\theta}(t) \approx A_2 \exp\left(-\frac{(\theta_m(t) - B_2)^2}{2(C_2)^2}\right). \quad (27)$$

Although θ_m and χ_{AG} are geometrically coupled, using distinct approximations enables a clear characterization of the individual influence of each variable on f while maintaining analytical tractability. This conditional approach allows the separate effects of altitude and elevation on the channel fading factor to be captured explicitly, without assuming statistical independence. The Gaussian approximations are physically motivated, capturing both monotonic and non-monotonic trends observed in the measured Rician-K factors for different UAV antenna placements, as detailed in Section V. The Gaussian fits demonstrate that these approximations provide a reliable and physically interpretable representation of the measured data.

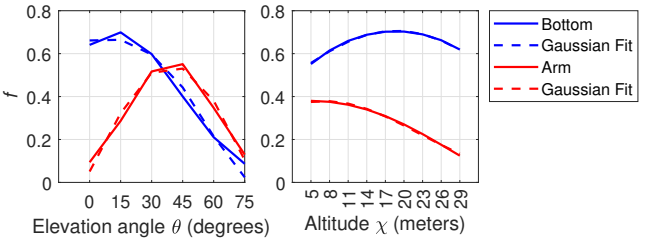

FIGURE 11: Effective fading power f versus θ and χ_{AG} with $\epsilon = 0.01$.

Consequently, we approximate the total effective fading power as $f_m(t) \approx f_m^{\theta}(t) \times f_m^{\chi_{AG}}(t)$. This multiplicative form is used as a tractable approximation and does not imply statistical independence between the two variables. The fitted Gaussian parameters $\{A_1, B_1, C_1, A_2, B_2, C_2\}$ in Fig. 11 are {0.70, 18.73, 19.83, 0.70, 12.86, 30.38} and {0.379, 7.22, 15.08, 0.57, 39.32, 20.68} in the Bottom and Arm antenna results, respectively. Next, the energy consumption of the SN can be written as $E_m = \int_{t=0}^{T_{\max}} x_m(t)(p_m(t) + p_c), \forall m$, where p_c corresponds to the circuit power of the SN during the wakeup mode which is a constant value. To ensure that UAV collects at least D_m bits from each SN in the mission time $T_{\max}$, we must have the following constraint.

$$\int_{t=0}^{T_{\max}} x_m(t) R_m(t) \ge D_m, \forall m \quad (28)$$

B. PROBLEM FORMULATION FOR EFFICIENT DATA COLLECTION

In this work, we consider the UG SNs that are powered by a battery with limited capacity to monitor soil conditions. It is crucial to note that, once the SNs are deployed, it is hard to recharge or replace the battery without removing the SNs from the soil. Considering the field deployment cost of each sensor, it is more important to optimize the resources on the SNs compared to the UAVs, to reduce energy consumption for operation time maximization. Moreover, it is also important to consider fairness among the SNs in terms of energy consumption during the data collection task because fair energy consumption of the SNs leads to similar operation times of the sensors. This helps to schedule maintenance of all the SNs at once. Accordingly, we consider an aerial data collection optimization problem that minimizes the maximum energy consumption among the SNs by jointly optimizing UAV 3D trajectory $(\mathbf{q}(t), \chi_{AG}(t))$, transmission scheduling $x_m(t)$, and uplink transmit power $p_m(t)$ while

satisfying the data collection requirement of each SN. Formally, the optimization problem can be written as follows.

$$P1: \min_{\substack{\xi,\mathbf{q}(t),\chi_{AG}(t),\\ p_m(t),x_m(t)}} \xi \tag{29}$$

$$s.t \quad E_m \le \xi, \forall m, \tag{30}$$

$$||v_{xy}(t)|| \le V_{xy}, ||v_z(t)|| \le V_z, \ \forall t, \tag{31}$$

$$(\mathbf{q}(0), \chi_{AG}(0)) = (\mathbf{q}^I, {\chi_{AG}}^I), \tag{32}$$

$$(\mathbf{q}(T_{\max}), \chi_{AG}(T_{\max})) = (\mathbf{q}^I, {\chi_{AG}}^I), \tag{33}$$

$$\chi_{AG\min} \le \chi_{AG}(t) \le \chi_{AG\max}, \forall t, \tag{34}$$

$$0 \le p_m(t) \le P_{\max}, \forall t, \forall m, \tag{35}$$

$$(21), (28),$$

where v_{xy} and v_z are the horizontal and vertical instantaneous velocity of the UAV, V_{xy} and V_z are the maximum horizontal and vertical velocity of the UAV, and $\chi_{AG\min}$ and $\chi_{AG\max}$ are the authority regulated minimum and maximum UAV altitudes, respectively. The constraints (32) and (33) ensure that the UAV takes off from the initial position $(\mathbf{q}^I, {\chi_{AG}}^I)$ at $t = 0$ and lands at the initial position at $t = T_{\max}$. The constraint (31) is the maximum velocity constraint on the UAV.

C. UAV-COLLECT

Note that the problem $P1$ is a mixed-integer non-convex problem, which is difficult to solve. Therefore, we approach this problem by adopting the fly, hover, and communicate protocol [21], [39], where the UAV flies to a set of hovering locations in a sequence and collects the data from each SN during the hover time. Then, the optimal trajectory is the UAV flying in a straight line between the hovering locations with the maximum horizontal and vertical speed (proof given in [21]). Let $\mathbf{\Lambda}$= $(\lambda_1,\ldots,\lambda_M)$ be the SN serving sequence of the UAV, $\hat{x}_m \in \{0,1\}$ be the SN wakeup schedule, $\hat{p}_{\lambda_m}$ be the average uplink power, and $(\mathbf{q}^H_{\lambda_m}, {\chi_{AG}}^H_{\lambda_m})$ and $\tau^H_{\lambda_m}$ be the hovering location and hovering time for the UAV to collect data from SN $\lambda_m, \forall m$, respectively. Then, the optimal serving sequence is the one that minimizes the total traveling distance of the UAV while ensuring that each hovering location is visited exactly once, which is equivalent to the traveling salesman problem (TSP) with M cities. Therefore, for a given set of hovering locations, $\mathbf{\Lambda}$ and $\hat{x}_m$ can be obtained by solving the TSP problem using efficient TSP solver algorithms to find approximate solutions [40]. Also, the optimal $\tau^H_{\lambda_m}$ is the one that satisfies that the D_{λ_m} bits are collected from the SN for a given rate R_{λ_m} i.e. $\tau^H_{\lambda_m} = D_{\lambda_m}/R_{\lambda_m}$. Therefore, for a given SN serving sequence $\mathbf{\Lambda}$, hovering time $\tau^H_{\lambda_m}$, and wakeup schedule $\hat{x}_m$, problem $P1$ can be reformulated as follows:

$$P2: \min_{\substack{\xi,\mathbf{q}^H_{\lambda_m},{\chi_{AG}}^H_{\lambda_m},\\ \hat{p}_{\lambda_m}}} \xi \tag{36}$$

$$s.t \quad \frac{D_{\lambda_m}}{R_{\lambda_m}}(\hat{p}_{\lambda_m} + p_c) \le \xi, \forall m, \tag{37}$$

$$\sum_{m=1}^{M} \frac{D_{\lambda_m}}{R_{\lambda_m}} + \sum_{m=1}^{M+1} \frac{||\mathbf{q}^H_{\lambda_m} - \mathbf{q}^H_{\lambda_{m-1}}||}{V_{xy}} + \frac{||{\chi_{AG}}^H_{\lambda_m} - {\chi_{AG}}^H_{\lambda_{m-1}}||}{V_z} \le T_{\max}, \tag{38}$$

$$\chi_{AG\min} \le {\chi_{AG}}^H_{\lambda_m} \le \chi_{AG\max}, \forall m, \tag{39}$$

$$0 \le \hat{p}_{\lambda_m} \le P_{\max}, \forall m, \tag{40}$$

where $\mathbf{q}^H_{\lambda_0} = \mathbf{q}^I, \mathbf{q}^H_{\lambda_{M+1}} = \mathbf{q}^I, {\chi_{AG}}^H_{\lambda_0} = {\chi_{AG}}^I, {\chi_{AG}}^H_{\lambda_{M+1}} = {\chi_{AG}}^I$, and (38) ensures that the total hovering time and flying time is less than the maximum flight time $T_{\max}$. The problem $P2$ is still non-convex because the R_{λ_m} is a non-convex function for the respective optimization variables. We approach problem $P2$ by dividing the problem into two sub-problems and solving them independently. For a fixed uplink power, problem $P2$ can be written as:

$$P2.1: \min_{\xi,\mathbf{q}^H_{\lambda_m},{\chi_{AG}}^H_{\lambda_m}} \xi \tag{41}$$

$$s.t \quad (37), (38), (39).$$

The problem $P2.1$ is still non-convex, and it is hard to find the optimal solution. Therefore, we solve the problem by adopting the augmented Lagrangian method (ALM) in which the constraints are augmented to the objective function to form a Lagrangian function. In particular, a quadratic penalty term is added to the Lagrangian function, which reduces the duality gap. ALM is based on the successive maximization of an augmented Lagrange function, in which the multipliers and the penalty parameters are fixed in each iteration, and then updated between iterations, until convergence. ALM can be applied to the problem $P2.1$ by minimizing the Lagrangian function given in (42), where $\boldsymbol{\pi} = [\pi_1, \ldots, \pi_M]$, Δ, $\boldsymbol{\iota} = [\iota_1, \ldots, \iota_M]$ are the Lagrange multipliers associated with constraints (37), (38) and (39), respectively, and Υ is the adjustable penalty parameter. The ALM consists of two main steps, where the first step deals with the minimization of $\mathcal{L}_{\boldsymbol{\pi},\Delta,\boldsymbol{\iota}}(\xi, \mathbf{q}^H_{\lambda_m}, {\chi_{AG}}^H_{\lambda_m})$ and second step deals with the update of the multipliers and penalty parameter. An iterative algorithm can be used to solve both the aforementioned steps until convergence. The Lagrange multipliers and penalty parameter at stage (l) are updated using (43)-(46), where $\pi_m^{(l+1)}$, $\iota_n^{(l+1)}$ and $\Delta^{(l+1)}$ are the updated values of Lagrange multipliers, $\Upsilon^{(l+1)}$ is the updated value of penalty parameter, and $\mathbf{q}^{H^{(l)}}_{\lambda_m}$ and ${\chi_{AG}}^{H^{(l)}}_{\lambda_m}$ are the optimized values of the horizontal and vertical location of the UAV at stage l, respectively. Note that to satisfy the lower bound of constraint (39), we select ${\chi_{AG}}^{H^{(l)}}_{\lambda_m} = \max(\chi_{AG\min}, {\chi_{AG}}'^{H^{(l)}}_{\lambda_m})$, where ${\chi_{AG}}'^{H^{(l)}}_{\lambda_m}$ is the optimized value calculated in the first step

(minimization) of ALM at stage l. In this way, the sub-optimal horizontal and vertical hovering positions, i.e., $\mathbf{q}_{\lambda_m}^{H^*}$ and ${\chi_{AG}}_{\lambda_m}^{H^*}$, are found.

For fixed horizontal and vertical hovering positions, problem $P2$ can be written as:

$$P2.2: \min_{\xi, \hat{p}_{\lambda_m}} \ \xi \quad (47)$$
$$s.t \qquad (37), (38), (40).$$

The problem $P2.2$ is non-convex due to the non-convex constraints (37). Therefore, we approach this problem by introducing the slack variables $\delta_{\lambda_m} > 0, \forall m$ and reformulating the problem as follows:

$$P2.3: \min_{\xi, \hat{p}_{\lambda_m}, \delta_{\lambda_m}} \ \xi \quad (48)$$
$$s.t \qquad \delta_{\lambda_m}(\hat{p}_{\lambda_m} + p_c) \leq \xi, \forall m, \quad (49)$$
$$\sum_{m=1}^{M} \delta_{\lambda_m} + \sum_{m=1}^{M+1} \frac{||\mathbf{q}_{\lambda_m}^H - \mathbf{q}_{\lambda_{m-1}}^H||}{V_{xy}} + \frac{||{\chi_{AG}}_{\lambda_m}^H - {\chi_{AG}}_{\lambda_{m-1}}^H||}{V_z} \leq T_{\max}, \quad (50)$$
$$0 \leq \hat{p}_{\lambda_m} \leq P_{\max}, \forall m, \quad (51)$$
$$\frac{D_{\lambda_m}}{R_{\lambda_m}} \leq \delta_{\lambda_m}, \forall m. \quad (52)$$

The problem $P2.3$ is convex for all the optimization variables and can be solved with standard convex solvers such as CVX [41]. By combining the solutions of each sub-problem, the problem $P2$ can be solved using Algorithm 1.

Algorithm 1 Algorithm to solve P2

1: Set $\mathbf{q}_{\lambda_m}^H = \mathbf{w}_{\lambda_m}$ and initial feasible value of $\hat{p}_{\lambda_m}$.
2: Find the SN serving sequence $\mathbf{\Lambda}$ and wake up schedule $\hat{x}_m$ using the TSP method.
3: Obtain the optimized horizontal $\mathbf{q}_{\lambda_m}^{H^*}$ and vertical ${\chi_{AG}}_{\lambda_m}^{H^*}$ hovering locations using ALM.
4: Obtain the optimized uplink power $\hat{p}_{\lambda_m}^*$ by solving problem P2.3 using a convex solver such as CVX.
5: Construct the UAV path incorporating the maximum flying speed and line segments, using the acquired serving sequence, hover positions, and hover durations.

D. EVALUATION OF OPTIMIZED UAV TRAJECTORIES

The performance of *UAV-Collect* is verified using the numerical simulation. We consider a system with multiple SNs with UG depths $\chi_{UG_m} = 0.1$ m, $\forall m$, which are randomly located in a 500×500 m^2 area as shown in Fig. 12a. We set $N_o = -110$ dBm, $\chi_{AG\min} = 5$ m, $\chi_{AG\max} = 29$ m, $V_{xy} = V_z = 50$ m/s, $W = 1$ MHz, $\eta = 2$, $P_{\max} = 1$ W, $p_c = 10^{-3}$ W, unit antenna gains, and rest of the effective fading and path loss model parameters from the Bottom antenna estimated results. The soil moisture value of the first SN that UAV visits is assumed to be 239 cB, and the rest of the SNs' soil moisture values are obtained using the spatial moisture correlation function ρ_s with $\rho_R = 0.01$. We consider the following two benchmark trajectory schemes for performance comparison: (i) Fixed location (FL): Where the hovering locations of the UAV in Algorithm 1 are fixed and set above the SNs (ii) Fixed Altitude (FA): Where only the altitude of the UAV is fixed in Algorithm 1.

The optimized trajectory of the UAV with the Algorithm 1 is shown for $M = 5$ SNs in Fig. 12a and the corresponding SNs' wakeup schedule is shown in Fig. 12b, where $T_{\max} = 60$ s and $D_{\lambda_m} = 1$ Mbits. It is observed that the UAV visits each SN and hovers at an optimized 3D position near the SN for a particular time, and the SNs are only woken up when the UAV reaches the corresponding hovering positions and remain silent otherwise. The performance comparison between *UAV-Collect* and benchmark methods

$$\mathcal{L}_{\boldsymbol{\pi},\Delta,\boldsymbol{\iota}}(\xi, \mathbf{q}_{\lambda_m}^H, {\chi_{AG}}_{\lambda_m}^H) = \xi + \frac{1}{2\Upsilon}\Bigg\{ \sum_{m=1}^{M}((\max\{0, \pi_m + \Upsilon(\frac{D_m}{R_m}(\hat{p}_m + p_c) - \xi)\})^2 - \pi_k^2) + ((\max\{0, \Delta + \Upsilon(\sum_{m=1}^{M}\frac{D_m}{R_m} + \sum_{m=1}^{M+1}\frac{||\mathbf{q}_{\lambda_m}^H - \mathbf{q}_{\lambda_{m-1}}^H||}{V_{xy}} + \frac{||{\chi_{AG}}_{\lambda_m}^H - {\chi_{AG}}_{\lambda_{m-1}}^H||}{V_z} - T_{\max})\})^2 - \Delta^2) + \sum_{m=1}^{M}(\max\{0, \iota_m - \Upsilon({\chi_{AG}}_{\lambda_m}^H - \chi_{AG\max})\})^2 - \iota_m^2)\Bigg\}, \quad (42)$$

$$\pi_m^{(l+1)} = \max\{0, \pi_m^{(l)} + \Upsilon^{(l)}(\frac{D_m}{R_m(\mathbf{q}_{\lambda_m}^{H^{(l)}})}(\hat{p}_m + p_c) - \xi^{(l)})\}, \forall m, \quad (43)$$

$$\Delta^{(l+1)} = \max\{0, \Delta + \Upsilon(\sum_{m=1}^{M}\frac{D_m}{R_m(\mathbf{q}_{\lambda_m}^{H^{(l)}})} + \sum_{m=1}^{M+1}\frac{||\mathbf{q}_{\lambda_m}^{H^{(l)}} - \mathbf{q}_{\lambda_{m-1}}^{H^{(l)}}||}{V_{xy}} + \frac{||{\chi_{AG}}_{\lambda_m}^{H^{(l)}} - {\chi_{AG}}_{\lambda_{m-1}}^{H^{(l)}}||}{V_z} - T_{\max})\} \quad (44)$$

$$\iota_m^{(l+1)} = \max\{0, \iota_n^{(l)} - \Upsilon({\chi_{AG}}_{\lambda_m}^{H^{(l)}} - \chi_{AG\max})\}, \forall m, \quad (45)$$
$$\Upsilon^{(l+1)} = 2\Upsilon^{(l)}, \quad (46)$$

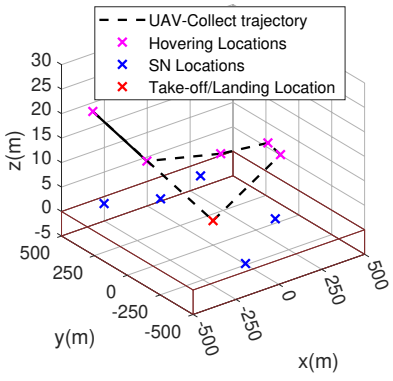

(a)

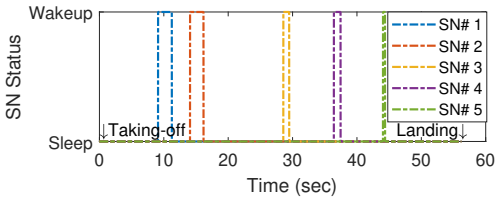

(b)

FIGURE 12: (a) UAV trajectory (b) SNs' wakeup schedule

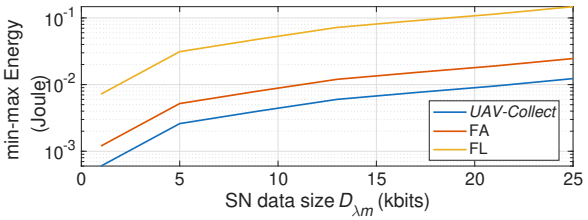

FIGURE 13: Min-max energy versus D_{λ_m} for $M = 100$ SNs

is shown for $M = 100$ SNs in Fig. 13, where the min-max energy consumption in each scheme is calculated for various values of D_{λ_m} with $T_{\max} = 20$ minutes. It can be seen that *UAV-Collect* outperforms all the benchmark schemes, and the performance gains are significant. This is because *UAV-Collect* finds the optimal hovering positions to communicate with each SN that provides the best channel conditions in terms of path loss and small-scale fading. Also, the comparison between FL and FA schemes shows that it is more important to optimize the horizontal position of the UAV than the altitude.

VII. CONCLUSION

In this study, the wireless channel characteristics between UAV and UG nodes are investigated using in-field outdoor measurements. The path loss and fading in the Air2UG and UG2Air channels are obtained at various altitudes and elevation angles, demonstrating the effect of soil depth, soil moisture, UAV 3D location, and UAV antenna position on signal propagation. Furthermore, the channels in both directions are comparable, and much like the Air2UG channel, the UG2Air channel's path loss depends on the incidence and refraction angles along the propagation path. Accordingly, a novel path loss model is proposed for Air2UG and UG2Air channels, which provides low estimation errors compared to the prior model in the literature. The small-scale fading distribution is analyzed at UAV and UG nodes that follow the Rician distribution. The Rician-K parameter is calculated and found to be significantly dependent on the UAV's altitude, elevation angle, and antenna position. Moreover, it is shown that the Gaussian function yields more accurate estimates of the Rician-K at various UAV 3D positions compared to the A2G exponential model. Moreover, the empirical findings and models are applied to a UAV-aided IoUT to determine an energy-efficient data collection strategy that satisfies the sensor data collection requirements. The numerical results demonstrate that the proposed scheme saves up to 12× amount of energy on the SNs compared to baseline schemes. Therefore, the suggested approach could potentially be applied to prolong the operational lifespan of the sensors in the soil during the planned data-collecting activities, in addition to expanding the coverage in IoUT.

REFERENCES

[1] M. C. Vuran, A. Salam, R. Wong, and S. Irmak, "Internet of underground things in precision agriculture: Architecture and technology aspects," Ad Hoc Networks, vol. 81, pp. 160–173, dec 2018.

[2] M. reza Akhondi, A. Talevski, S. Carlsen, and S. Petersen, "Applications of wireless sensor networks in the oil, gas and resources industries," in 2010 24th IEEE International Conference on Advanced Information Networking and Applications. IEEE, 2010, pp. 941–948.

[3] "GroGru products," https://www.groguru.com/products/.

[4] M. A. Akkaş, I. F. Akyildiz, and R. Sokullu, "Terahertz channel modeling of underground sensor networks in oil reservoirs," in 2012 IEEE Glob. Commun. Conf. IEEE, 2012, pp. 543–548.

[5] M. C. Vuran and I. F. Akyildiz, "Channel model and analysis for wireless underground sensor networks in soil medium," Physical communication, vol. 3, no. 4, pp. 245–254, 2010.

[6] Z. Sun, P. Wang, M. Vuran, M. Al-Rodhaan, A. Al-Dhelaan, and I. Akyildiz, "Mise-pipe: Magnetic induction-based wireless sensor networks for underground pipeline monitoring," Ad Hoc Networks, vol. 9, no. 3, pp. 218–227, 2011.

[7] Z. Sun and I. F. Akyildiz, "Connectivity in wireless underground sensor networks," in 2010 7th Annual IEEE SECON. IEEE, 2010, pp. 1–9.

[8] A. Salam, M. C. Vuran, X. Dong, C. Argyropoulos, and S. Irmak, "A theoretical model of underground dipole antennas for communications in internet of underground things," IEEE Trans. Antennas Propag., vol. 67, no. 6, pp. 3996–4009, jun 2019.

[9] "Soil Scout wireless soil moisture sensor," https://soilscout.com/solution/wireless-soil-moisture-sensor.

[10] "Linovision wireless soil moisture sensor," https://linovision.com/products/.

[11] S. M. Hashir, M. C. Vuran, and J. Camp, "Echo: Empirical characterization and height optimization of uav-to-underground channels," in 2023 IEEE PIMRC, 2023, pp. 1–7.

[12] S. Jamil, Fawad, M. Rahman, A. Ullah, S. Badnava, M. Forsat, and S. S. Mirjavadi, "Malicious uav detection using integrated audio and visual features for public safety applications," Sensors, vol. 20, no. 14, p. 3923, 2020.

[13] A. Silva and M. Vuran, "Communication with aboveground devices in wireless underground sensor networks: An empirical study," in IEEE Int. Conf. on Commun., 2010.

[14] X. Dong, M. C. Vuran, and S. Irmak, "Autonomous precision agriculture through integration of wireless underground sensor networks with center pivot irrigation systems," Ad Hoc Networks, vol. 11, no. 7, pp. 1975–1987, 2013.

[15] A. Salam, M. C. Vuran, and S. Irmak, "A statistical impulse response model based on empirical characterization of wireless underground channels," IEEE Trans. Wirel. Commun., vol. 19, no. 9, pp. 5966–5981, 2020.
[16] L. Holtorf, I. Titov, F. Daschner, and M. Gerken, "Uav-based wireless data collection from underground sensor nodes for precision agriculture," AgriEngineering, vol. 5, no. 1, pp. 338–354, 2023.
[17] C. Cariou, L. Moiroux-Arvis, F. Pinet, and J.-P. Chanet, "Data collection from buried sensor nodes by means of an unmanned aerial vehicle," Sensors, vol. 22, no. 15, p. 5926, 2022.
[18] M. Rahman, M. J. Khan, M. A. Asghar, Y. Amin, S. Badnava, S. S. Mirjavadi et al., "Image local features description through polynomial approximation," IEEE Access, vol. 7, pp. 183 692–183 705, 2019.
[19] C. You and R. Zhang, "3d trajectory optimization in rician fading for uav-enabled data harvesting," IEEE Transactions on Wireless Communications, vol. 18, no. 6, pp. 3192–3207, 2019.
[20] C. Zhan, Y. Zeng, and R. Zhang, "Energy-efficient data collection in uav enabled wireless sensor network," IEEE Wireless Communications Letters, vol. 7, no. 3, pp. 328–331, 2017.
[21] C. Zhan and Y. Zeng, "Completion time minimization for multi-uav-enabled data collection," IEEE Transactions on Wireless Communications, vol. 18, no. 10, pp. 4859–4872, 2019.
[22] Y. Zhu, B. Yang, M. Liu, and Z. Li, "Uav trajectory optimization for large-scale and low-power data collection: An attention-reinforced learning scheme," IEEE Transactions on Wireless Communications, vol. 23, no. 4, pp. 3009–3024, 2024.
[23] K.-V. Nguyen, C.-H. Nguyen, T. V. Do, and C. Rotter, "Efficient multi-uav assisted data gathering schemes for maximizing the operation time of wireless sensor networks in precision farming," IEEE Transactions on Industrial Informatics, vol. 19, no. 12, pp. 11 664–11 674, 2023.
[24] L. Li, M. C. Vuran, and I. F. Akyildiz, "Characteristics of underground channel for wireless underground sensor networks," in Proc. Med-Hoc-Net, vol. 7, 2007, pp. 13–15.
[25] N. R. Peplinski, F. T. Ulaby, and M. C. Dobson, "Dielectric properties of soils in the 0.3-1.3-ghz range," IEEE Trans. Geosci. Remote Sens., vol. 33, no. 3, pp. 803–807, 1995.
[26] X. Dong and M. C. Vuran, "Impacts of soil moisture on cognitive radio underground networks," in 2013 first international black sea conference on communications and networking (BlackSeaCom). IEEE, 2013, pp. 222–227.
[27] Q. Feng, J. McGeehan, E. K. Tameh, and A. R. Nix, "Path loss models for air-to-ground radio channels in urban environments," in 2006 IEEE 63rd vehicular technology conference, vol. 6. IEEE, 2006, pp. 2901–2905.
[28] A. Al-Hourani and K. Gomez, "Modeling cellular-to-uav path-loss for suburban environments," IEEE Wireless Communications Letters, vol. 7, no. 1, pp. 82–85, 2017.
[29] Z. Qiu, X. Chu, C. Calvo-Ramirez, C. Briso, X. Yin et al., "Low altitude uav air-to-ground channel measurement and modeling in semiurban environments," Wireless Communications and Mobile Computing, vol. 2017, 2017.
[30] S. Shimamoto et al., "Channel characterization and performance evaluation of mobile communication employing stratospheric platforms," IEICE transactions on communications, vol. 89, no. 3, pp. 937–944, 2006.
[31] M. Badi, J. Wensowitch, D. Rajan, and J. Camp, "Experimentally analyzing diverse antenna placements and orientations for uav communications," IEEE Transactions on Vehicular Technology, vol. 69, no. 12, pp. 14 989–15 004, 2020.
[32] M. C. Vuran, X. Dong, and D. Anthony, "Antenna for wireless underground communication," Grant US 9 532 118, Dec. 27, 2016.
[33] J. Chard, "Watermark soil moisture sensors: characteristics and operating instructions," Utah State University, 2002.
[34] A. Salam, M. C. Vuran, X. Dong, C. Argyropoulos, and S. Irmak, "A theoretical model of underground dipole antennas for communications in internet of underground things," IEEE Trans. Antennas Propag., vol. 67, no. 6, pp. 3996–4009, 2019.
[35] S. Büyükçorak, M. Vural, and G. K. Kurt, "Lognormal mixture shadowing," IEEE Transactions on Vehicular Technology, vol. 64, no. 10, pp. 4386–4398, 2015.
[36] V. Isham, D. Cox, I. Rodriguez-Iturbe, A. Porporato, and S. Manfreda, "Representation of space–time variability of soil moisture," Proceedings of the Royal Society A: Mathematical, Physical and Engineering Sciences, vol. 461, no. 2064, pp. 4035–4055, 2005.
[37] I. Rodríguez-Iturbe, V. Isham, D. Cox, S. Manfreda, and A. Porporato, "Space-time modeling of soil moisture: Stochastic rainfall forcing with heterogeneous vegetation," Water resources research, vol. 42, no. 6, 2006.
[38] M. M. Azari, F. Rosas, K.-C. Chen, and S. Pollin, "Ultra reliable uav communication using altitude and cooperation diversity," IEEE Transactions on Communications, vol. 66, no. 1, pp. 330–344, 2017.
[39] Y. Zeng, J. Xu, and R. Zhang, "Energy minimization for wireless communication with rotary-wing uav," IEEE transactions on wireless communications, vol. 18, no. 4, pp. 2329–2345, 2019.
[40] R. Matai, S. P. Singh, and M. L. Mittal, "Traveling salesman problem: an overview of applications, formulations, and solution approaches," Traveling salesman problem, theory and applications, vol. 1, no. 1, pp. 1–25, 2010.
[41] M. Grant and S. Boyd, "Cvx: Matlab software for disciplined convex programming, version 2.1," 2014.

SYED MUHAMMAD HASHIR received the B.E. degree in Electronics Engineering from the Karachi Institute of Economics and Technology, Karachi, Sindh, Pakistan, the M.S. degree in Electrical, Electronics, and Cyber Systems from Istanbul Medipol University, Istanbul, Turkey, and the Ph.D. degree in Electrical Engineering from Southern Methodist University, Dallas, TX, USA. He is currently an Assistant Professor in the Department of Engineering Technology at the University of Kentucky, Paducah, KY, USA. His current research interests include unmanned aerial vehicles (UAVs), underground wireless sensor networks, and the integration of wireless communication and aerial technologies to enhance precision agriculture.

MEHMET C. VURAN earned his B.S. in Electrical and Electronics Engineering from Bilkent University, Turkey in 2002 and his M.S. and Ph.D. in Electrical and Computer Engineering from Georgia Institute of Technology in 2004 and 2007, respectively. Currently, he is the Dale M. Jensen Professor of Computing at the University of Nebraska-Lincoln. Dr. Vuran received an NSF CAREER (2010) for "Bringing Wireless Sensor Networks Underground" and was recognized as a Highly Cited Researcher in Computer Science three years in a row by Thomson Reuters, ranking in the top 1% of researchers for most cited documents in the field. He is a National Strategic Research Institute Fellow and a Daugherty Water for Food Global Institute Fellow. Dr. Vuran is the co-author of the textbook "Wireless Sensor Networks". He has served as the TPC Co-Chair of IEEE INFOCOM 2020 and on the editorial boards of IEEE Transactions on Wireless Communications, IEEE Transactions on Mobile Computing, and IEEE Communications Surveys and Tutorials Journal. His research interests include the Internet of Things, wireless underground sensing and communications, mmWave and THz sensing and communications in challenging environments, dynamic spectrum access, connected autonomous systems, and cyber-physical networking.

This article has been accepted for publication in IEEE Access. This is the author's version which has not been fully edited and content may change prior to final publication. Citation information: DOI 10.1109/ACCESS.2026.3697971

DINESH RAJAN received his B.Tech degree from Indian Institute of Technology (IIT), Madras in Electrical Engineering. He was also awarded the M.S and Ph.D degrees from Rice University, Houston, Texas both in the areas of Electrical and Computer Engineering. He joined Southern Methodist University (SMU) in 2002 as an Assistant Professor. He was Department Chair in the Department of Electrical and Computer Engineering at SMU, from 2012 to 2022. He is currently Associate Dean and Cecil and Ida Green Professor in the Lyle School of Engineering at SMU. Dr. Rajan's broad interests are in the sensing, extraction, transmission, and dissemination of information. His current research is interdisciplinary and spans the traditional areas of communications theory, wireless networks, information theory, system optimization, and computational imaging.

MANINDERPAL SINGH is an IEEE member and is with the University of Houston, where he explores developments in Internet of Things (IoT) systems. He completed his postdoctoral fellowship at Southern Methodist University, contributing to advanced research in intelligent networks, spectrum allocation optimization. His current work centers on generative intelligence, edge intelligence, network optimization, and security within IoT domains. He actively contributes to the academic community through peer-reviewed publications and manuscript reviews.

JOSEPH D. CAMP received the B.S. (Hons.) degree in electrical and computer engineering from The University of Texas at Austin and the M.S. and Ph.D. degrees in electrical and computer engineering from Rice University, Houston, TX, USA. He is a Professor of Electrical and Computer Engineering and Director of the Autonomous Drone Teaming Lab at Southern Methodist University, Dallas, TX, USA. His research team has performed over 200 million in-field wireless measurements using drones and mobile devices. His interests include wireless communications and networking, AI-driven optimization, and blockchain-secured coordination for autonomous systems. Dr. Camp received the Ralph Budd Award (2010), NSF CAREER Award (2012), Golden Mustang Teaching Award (2014), Gerald J. Ford Research Fellowship (2021), and the IEEE LATINCOM Best Paper Award (2022).